Journal of Wind Engineering & Industrial Aerodynamics 206 (2020) 104332

Contents lists available at ScienceDirect

Journal of Wind Engineering & Industrial Aerodynamics

journal homepage: www.elsevier.com/locate/jweia

Vertical profile characteristics of thunderstorm outflows

Federico Canepa *, Massimiliano Burlando, Giovanni Solari

Department of Civil, Chemical and Environmental Engineering, Polytechnic School, University of Genoa, Genoa, Italy

ARTICLE INFO

Keywords:
Downburst
Field measurements
LiDAR
Mediterranean
Nose shape profile
Thunderstorm
Turbulence
Vertical profile

ABSTRACT

The dynamic complexity and the limited spatiotemporal structure of thunderstorms make the collection of reliable and systematic measurements of this phenomenon, which are definitely needed to evaluate its action on structures, challenging. The Northern Tyrrhenian is a "hot-spot" for the genesis of severe potentially damaging wind phenomena, such as downbursts. In the context of the European projects "Wind and Ports" and "Wind, Ports and Sea", a large and complex wind monitoring network has been installed just in this area. Here, three LiDAR profilers provide a vertical scanning of the atmosphere up to 250 m above the ground level. From their continuous recordings, a method to extract thunderstorm events is herein proposed, based on an automated procedure involving systematic quantitative controls and specific qualitative judgments. Starting from it, this paper provides a comprehensive investigation and comparison of the main parameters ruling the outflow vertical profiles of a selected subset of thunderstorms. The nose shape of the wind profiles appears mainly during the velocity ramp-up and peak stages. During the downburst, the wind direction is systematically invariant with height. The capability of LiDAR to measure the wind speed turbulence component is also discussed and its properties along the vertical profile are shown.

1. Introduction

Despite an impressive amount of research, a shared model for thunderstorm-induced actions on structures is not available yet, mainly because the complexity of thunderstorms makes it difficult to establish physically realistic and simple models as in the case of extra-tropical cyclones (Solari, 2019); so, the methods currently applied to determine the wind actions on structures are still referred to the synoptic-scale extra-tropical cyclones that strike mid-latitude areas (Davenport, 1967). Unfortunately, thunderstorms present time-space characteristics completely different from extra-tropical cyclones and in many cases their intensity exceeds that of synoptic events. Thom (1968) first showed that one-third of the yearly peak wind velocities in the United States occur during thunderstorms, which are, in fact, the dominant wind type for structural design in many parts of the world (Gomes and Vickery, 1978; Letchford et al., 2002). Zhang et al. (2018a) also showed that design wind velocities with mean return period greater than 10–20 years are often associated with thunderstorms.

These phenomena are made up of sets of cells that evolve through three stages in about 30 minutes: cumulus, mature and dissipating stages (Byers and Braham, 1948). Fujita (1981, 1985) showed that the downdraft that impinges over the ground produces intense non-stationary radial outflows and ring vortices. The whole of this air movement is called "downburst" and it can be divided into "macro-burst" and "micro-burst" depending on whether its horizontal size is greater or smaller than 4 km, respectively. The research carried out in wind engineering during the last two decades has demonstrated that downbursts, and especially micro-bursts, are extremely damaging not only with regard to flights but, indeed, also for the built environment (e.g. Holmes et al., 2008; Solari et al., 2012, 2015b; Elawady et al., 2017).

According to this finding, many attempts have been carried out to analyse thunderstorm measurements and to obtain the parameters of major interest for evaluating their actions on structures (Goff, 1976; Wakimoto, 1982; Choi, 1999, 2004; Choi and Hidayat, 2002; Gunter and Schroeder, 2015). Nevertheless, there is still a great number of unknown facets associated with downbursts. The parameters of major interest for wind engineering purposes are difficult to generalize at the global scale and their variability is often very large; downburst properties such as the jet diameter, the spatial and temporal extension of the phenomenon or its intensity at the near-ground levels are event-dependent and vary significantly according to mesoscale and regional climate as well as to the type of thunderstorm cell. In addition, the interaction between the small scale downburst and the large scale synoptic wind as well as the motion of the parent cloud is an open topic, currently under investigation (Romanic

* Corresponding author.
E-mail address: federico.canepa@edu.unige.it (F. Canepa).

https://doi.org/10.1016/j.jweia.2020.104332
Received 23 January 2020; Received in revised form 31 July 2020; Accepted 1 August 2020
Available online xxxx

et al., 2017; Romanic and Hangan, 2019).

Besides this, the lack of information depends mainly on two aspects: firstly, high-sampling-rate anemometric sensors are needed to catch the evolution in time of thunderstorms, but this kind of sensors is not the standard in meteorological stations; secondly, the small size of thunderstorms in respect to met-stations spacing makes these objects most often undetected at the ground. It follows that, in view of providing a complete reconstruction of these phenomena, the available data for thunderstorms are still very limited compared to synoptic events, pointing out the necessity of collecting and analysing as many thunderstorm records as possible (Burlando et al., 2017b). In this perspective, a great contribution has been recently given by the extensive anemometric network realized for the European projects "Wind and Ports" (WP, 2009–2012) (Solari et al., 2012) and "Wind, Ports and Sea" (WPS, 2013–2015) (Repetto et al., 2018). This network is expected to contribute in reducing the lack of knowledge and the uncertainties on the physical behavior of downbursts, which are the main focus of the recently launched ERC Project THUNDERR – "Detection, simulation, modelling and loading of thunderstorm outflows to design wind-safer and cost-efficient structures" (2017–2022) (Solari et al., 2020).

The analysis of the field data acquired for the projects WP and WPS represents a unique opportunity to reconstruct the time and spatial evolution of small-scale storms. The three WindCube LiDAR wind vertical profilers which belong to the anemometric network, in particular, can be used to characterise the vertical development of thunderstorm outflows. This analysis is expected to lead, among other benefits, to the definition of the range of heights where the maximum wind speeds are experienced, investigating the transient nose-like shape assumed by the velocity vertical profile (Goff, 1976). In this framework, literature has largely documented that the vigorous horizontal wind speeds, originated upon the jet impingement, present their maxima close to the ground in the interval 50–120 m above ground level (AGL) with related implications for low/mid-rise structures. This is noticeable only by analysing the vertical profile of the slowly-varying mean wind velocity component in the stage of the maximum intensity of the outflow. The usual 10-min average applied to synoptic event time-series completely filters out such features. From LiDAR measurements and their comparison with meteorological information, it can be noted that the long-lasting nose--like shape profiles of the order of 10-min or more, are never associated with thunderstorm events. They occur, for example, when stable atmospheric conditions prevent deep convection, such as in downslope winds (Burlando et al., 2017c). Conversely, short-lasting nose shapes, in the order of 1-min, are observed during thunderstorms (Burlando et al., 2017a).

The present paper extends on the study by Burlando et al. (2017a), where a first set of thunderstorm measurements was extracted and studied during the period 2014–2015. Such investigation is here enlarged until mid-2018. Three LiDAR (Light Detection and Ranging) databases of continuous wind records are systematically analysed to extract the records which may relate to thunderstorm events. This is confirmed through subjective inspections of the signals and cross-checking interpretations of satellite, radar and lightning data. The wind data are processed through the directional decomposition technique proposed by Zhang et al. (2019), which allows, on the one hand, to address the abrupt change in direction during thunderstorm events with the same approach used for the wind speed component and, on the other hand, to decouple the turbulent fluctuations into longitudinal and lateral components. The downburst signals are analysed to inspect the time transition of the wind speed and direction vertical profile, the duration of the nose-shaped profile, the gust factor, and the directional shift. The reliability of the LiDAR vertical profilers to detect the turbulence component of the flow is discussed in relation to literature reviews; the related properties are therefore analysed with regard to their time evolution along the height.

The rest of this paper develops through the following sections: Section 2 describes the wind monitoring network developed for the projects WP and WPS along with a detailed overview of the LiDAR wind profilers. The definition of the signal decomposition techniques and the extraction criterion here adopted are presented in Section 3. Section 4 describes, in detail, the thunderstorm event that occurred in Livorno on September 13, 2015. Section 5 discusses the main analogies and differences among the investigated events in terms of vertical profiles of the slowly-varying mean wind speed, direction and turbulence intensity. Conclusions and future prospects are reported in Section 6.

2. Wind monitoring network and Lidar profilers

WP and WPS are two projects financed by the European Territorial Cooperation Objective, Cross-border program "Italy-France Maritime 2007–2013". An extensive in-situ wind monitoring network made up of 28 ultrasonic anemometers, three meteorological stations and three LiDAR profilers, has been installed in the main commercial ports of the Northern Tyrrhenian and Ligurian Sea: Savona/Vado Ligure, Genoa, La Spezia, Livorno, Bastia and L'Ile Rousse. This has allowed to collect an unprecedented dataset of wind measurements, to develop numerical simulations of wind and wave fields, the statistical analysis of the wind climate, and algorithms for medium term (1–3 days) and short term (0.5–2 h) wind forecasts.

The large anemometric network provided by the projects WP and WPS has been regularly enriched with the introduction of new measuring instruments. In this sense, the project THUNDERR has recently provided a further significant contribution; to be mentioned, among others, the installation of a state-of-the-art pulsed LiDAR scanner, not treated in this study.

The three LiDAR wind profilers, installed in the ports of Genoa, Livorno and Savona, are here investigated. They measure the three components of the wind velocity at 12 heights AGL (40, 50, 60, 80, 90, 100, 120, 140, 160, 180, 200, 250 m) with a sampling rate of 1 Hz, providing a continuous reconstruction of the wind speed vertical profile. A ground ultrasonic anemometer is always supplied in the proximity of the LiDAR system, usually at about 10 m AGL, providing the field reconstruction from the lower levels. The overall system in the three ports where the LiDARs are located is reported in Fig. 1.

The three LiDARs were installed in the years 2014–2015 (codes GE.51, LI.51 and SV.51). The first of the three was launched in Savona in the second quarter of 2014. The remaining two (Genoa and Livorno) were installed approximately one year later. The related databases of measurements cover different periods according to their installation date until August 31, 2018, which is the last date considered in the present analysis. The discontinuities in the data acquisition have to be addressed to malfunctioning, ordinary maintenance and, in the case of LI.51, to vandalism attack. Other lacks of recorded data are, instead, to be related to heavy precipitations, which prevent the instrument to acquire useful information often reducing the maximum height of measurements because of the scattering due to water raindrops.

Each of the 3 LiDARs investigated here is a ground-based pulsed coherent system manufactured by Leosphere and whose commercial name is "WindCube V2". It produces regularly spaced emissions of highly collimated light energy for a specified period of time (pulse length). For each azimuth angle, the line-of-sight velocity, i.e. the radial velocity v_r, is calculated based on the principle of the Doppler shift in the frequency of the received radiation or, in other words, the time shift of the back-scattered light.

At a fixed vertical angle usually equal to 30°, the instrument measures four sequential radial velocities $v_{r,\theta}$ around the circle formed by a conical scanning, i.e. $\theta = 0°$, 90°, 180° and 270° plus one vertical measurement above the LiDAR itself. The time step between two subsequent pulses is 1-s which leads to record a complete conical scanning in 5-s. The three components of the velocity are then derived and, assuming the horizontal homogeneity of the wind field over the sensed height, the wind velocity vector can be considered as representative of the central point of the circle (Fig. 2).

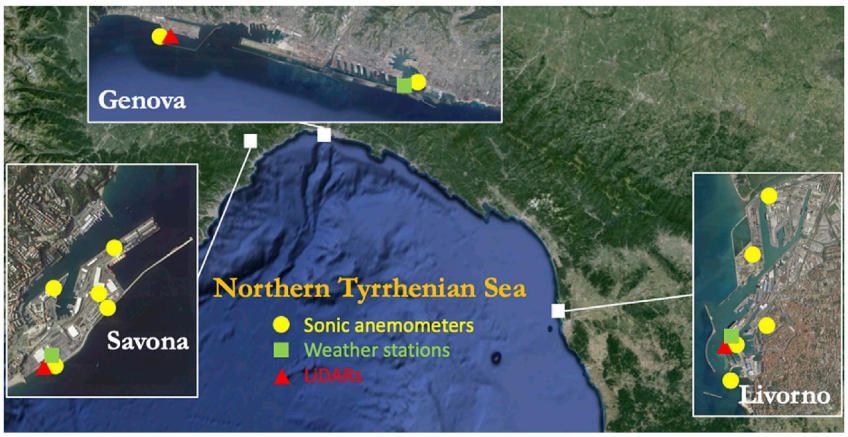

Fig. 1. Monitoring network in the Ports of Savona, Genoa and Livorno.

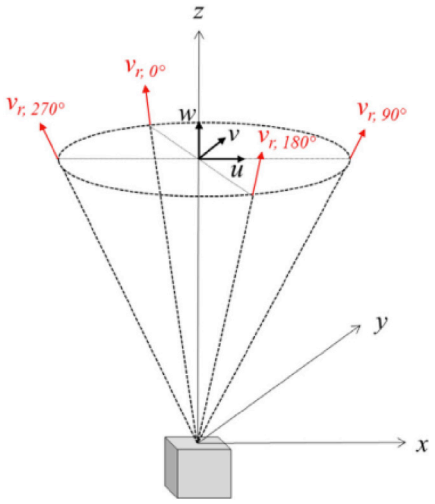

Fig. 2. Scheme of the LiDAR and scanning method.

All the wind speed measurements at a certain azimuth angle are acquired simultaneously along the vertical profile due to the pulsed nature of the system. Other commercial LiDAR profilers, such as the ZephIR system, perform continuous conical scannings from the bottom to the top height; however, the non-simultaneity of the recorded profiles make this type of LiDAR less suited for engineering purposes, especially in the light of reconstructing transient events such as downbursts. The LiDARs treated in this study measure with a sensitivity of 0.1 m/s and 2° for the wind speed and direction, respectively. The variance of the recorded velocity is influenced by the volume filtering operated by the system which, however, can be predicted and partly corrected theoretically. LiDAR reconstructs the wind speed at each sensed height by averaging the above-mentioned five 1-Hz measurements; thus, it takes into account the width and depth of the resultant cone of measurements which increases in size with the elevation. LiDAR presents the limit of the non-independency of such measurements which later are brought together to re-compose the resultant radial velocity at the central point of the circle: every second in time the instrument performs a single individual azimuthal measurement and assembles this with the four previous ones. For this reason, none of the radial velocities can be dealt with as independent from both the preceding and following. However, the comparison between anemometric and LiDAR time-series shows a very good agreement at time scales of the order of 2 s.

The accuracy of LiDAR measurements of mean wind velocity profiles is proven (Wilczak et al., 1996; Smith et al., 2006), whereas the reliability of turbulence measurements is still controversial (Sathe et al., 2011; Sathe and Mann, 2013). However, the bias depends strongly on the spatial structure of turbulence, which changes largely with the atmospheric stability. The unstable condition of the atmosphere during downburst events leads to large eddy structures; they form, in fact, as a consequence of the environmental instability between the denser descending current and the surrounding air. The full scale investigation carried out by Sathe et al. (2011) shows how this turbulence configuration provides a significant decrease of the systematic error, defined as the ratio of the LiDAR second-order moments, $\overline{u'u'}$ and $\overline{u'w'}$, to the same "true" second-order moments as measured by sonic anemometers, which assumes values close to 1 above 60 m AGL (Mann et al., 2010). Considering the validity and reliability of the turbulence intensity as acquired by the LiDAR, its properties are here investigated to provide a picture of their behavior along the sensed measurement heights. The results were eventually compared to the same quantities evaluated from sonic and ultrasonic measurements during previous full-scale campaigns (Zhang et al., 2018b, 2019) in order to inspect their mutual similarity. This may somehow and qualitatively confirm the goodness of LiDAR to detect the turbulent part of the wind signal in terms of overall statistical moments whereas it remains highly questionable the possibility of performing time-based analyses and thus synthesizing its harmonic content for instance with reference to a power spectral density or a coherence function.

Leosphere WindCube LiDARs are not designed for measuring at elevations lower than 40 m AGL due to the potential noise in the back-scattered signal. This is mainly due to the lens and to the sealing window of the instrument which reflect the emitted radiation and generate noise that cannot be filtered out at the lower heights due to the short time interval elapsing before the signal is received back. Instead, the upper limit of 250 m AGL is related to the power of the laser beam emitted by the instrument. However, at the higher measurement heights, the density of available aerosol parcels decreases in the atmosphere and, sometimes, the reflected laser beam sent back to the LiDAR is too weak to be measured by the instrument. This is even more noticeable during wet downbursts, which surely represent the vast majority of thunderstorm events in the area of the Northern Tyrrhenian Sea (Burlando et al., 2018). Here, the heavy rain embedded in the downdraft region during the event strongly interferes with the signal emitted by the LiDAR while, after the passage of the storm, the higher atmospheric levels below and behind the cumulonimbus cloud base are densely populated by rain drops not yet evaporated which, therefore, contribute to make the air extremely clean and thus poor of aerosols through atmospheric scavenging.

3. Data extraction and analysis

The method here adopted to extract thunderstorms involves parameters related to the modulus of the wind speed $U(t)$, defined according to

the classical decomposition method for downbursts which is shortly described in Section 3.1. Besides it, the obtained signals are processed by means of the novel directional technique (Zhang et al., 2019) with the benefits described in Section 3.2. Section 3.3 briefly presents the two main families of criteria to extract thunderstorm records from large wind datasets with focus on the technique used by the authors in the current study. The resulting events are thus shown and the values of the parameters involved in the extraction method are reported for each event.

3.1. Classical decomposition

This approach (Chen and Letchford, 2005; Holmes et al., 2008) consists of decomposing the resultant horizontal wind speed U:

$$U(t) = \sqrt{V_X^2(t) + V_Y^2(t)} \tag{1}$$

into a slowly-varying mean velocity $\overline{U}$ and a fluctuation U' that is expressed as the product of the slowly-varying standard deviation σ_U by a reduced turbulent fluctuation $\tilde{U}$' dealt with as a stationary Gaussian random process with zero mean and unit standard deviation. In Eq. (1) t is the time, while V_X and V_Y are the horizontal components of the wind speed. So, the resultant velocity may be expressed as:

$$U(t) = \overline{U}(t) + U'(t) = \overline{U}(t) + \sigma_U(t)\tilde{U}'(t) = \overline{U}(t)\,[1 + \ I_U(t)\ \tilde{U}'(t)] \tag{2}$$

$I_U(t) = \sigma_U(t)/\overline{U}(t) = \bar{I}_U\mu_U(t)$ being the slowly-varying turbulence intensity, $\bar{I}_U$ is the mean value of I_U whereas μ_U is a non-dimensional function of t that describes the slow variation of I_U with $\overline{\mu}_U = 1$. In this paper, all the slowly-varying quantities are determined through a moving average filter with a moving average period $T = 30\,s$ (Solari et al., 2015a).

3.2. Directional decomposition

This approach (Zhang et al., 2019) consists of decomposing the wind speed components (V_X, V_Y) into the slowly-varying mean $(\overline{V}_X, \overline{V}_Y)$ and the residual fluctuation (V_X', V_Y') components. The resultant slowly-varying mean wind speed is given by:

$$\overline{u}(t) = \sqrt{\overline{V}_X^2(t) + \overline{V}_Y^2(t)} \tag{3}$$

The slowly-varying direction of $\overline{u}$, according to the geographical notation, is identified by the angle $\overline{\alpha} \in [0, 360]$ defined as:

$$\overline{\alpha}(t) = 270 - \text{atan2}\left[\frac{\overline{V}_Y(t)}{\overline{V}_X(t)}\right] \tag{4}$$

The residual fluctuation is projected onto a new Cartesian reference system (x, y) where the x-axis is aligned with $\overline{u}$ and is rotated $\overline{\beta} = \overline{\beta}(t) = 270 - \overline{\alpha}(t)$ with respect to the fixed X-axis. Thus:

$$u'(t) = V_x'(t)\cos\overline{\beta}(t) + V_y'(t)\sin\overline{\beta}(t) \ \ ; \ \ v'(t) = -V_x'(t)\sin\overline{\beta}(t) + V_y'(t)\cos\overline{\beta}(t) \tag{5}$$

where u' and v' are the longitudinal and lateral turbulence components, respectively. They are expressed as the product of their slowly-varying standard deviations (σ_u, σ_v) by a couple of longitudinal and lateral reduced turbulent fluctuations $(\tilde{u}', \tilde{v}')$ dealt with as stationary Gaussian non-correlated random processes with zero mean and unit standard deviation:

$$u'(t) = \sigma_u(t)\tilde{u}'(t) \quad ; \quad v'(t) = \sigma_v(t)\tilde{v}'(t) \tag{6}$$

Accordingly, the longitudinal and lateral components of the wind velocity may be expressed as:

$$u(t) = \overline{u}(t) + u'(t) = \overline{u}(t)\,[1 + \ I_u(t)\ \tilde{u}'(t)] \ \ ; \ \ v(t) = v'(t) = \overline{u}(t)\,I_v(t)\,\tilde{v}'(t) \tag{7}$$

where $I_u(t) = \sigma_u(t)/\overline{u}(t) = \bar{I}_u\mu_u(t)$ and $I_v(t) = \sigma_v(t)/\overline{u}(t) = \bar{I}_v\mu_v(t)$ are respectively, in analogy with Section 3.1, the longitudinal and lateral slowly-varying turbulence intensities.

This approach contains the classical decomposition as a particular case, establishes a perfect parallelism with the classical decomposition of synoptic wind speed records, provides substantial advantages for the reconstruction of detected moving downbursts as well as for evaluating the dynamic response of structures in terms of alongwind and crosswind vibrations, as this is classical for synoptic winds.

3.3. Wind data separation and classification method

The methods to separate thunderstorm from non-thunderstorm events may be subdivided into two families mainly associated with the meteorological and wind engineering fields: the first family identifies thunderstorm events by detailed inspections and reconstructions of the meteorological conditions, relying on surface measurements of the main meteorological parameters, radar and satellite images, soundings and other suitable data (Geerts, 2001; Gast and Schroeder, 2003); the second family is based on the signal analysis and the resultant systematic separation and classification of measurements belonging to large datasets, with the purpose of performing statistical analyses of the extreme wind velocities and their effects on structures. Since the continuous acquisition of measurements leads to the formation and constant growth of very large wind signal databases, the latter methods avoid to provide a detailed meteorological investigation and representation of all wind events, in favor of an automated, systematic and fast procedure to separate and classify the recorded events into sub-datasets (Kasperski, 2002; Durañona et al., 2007; De Gaetano et al., 2014).

The extremely large amount of data examined in the present study led to adopt a separation method belonging to this latter class of criteria rather than a purely meteorological one. All the available data were systematically analysed in order to detect those events that were believed to be thunderstorms. The first preliminary selection is based on the following analytical criteria:

- 10-min maximum 1-Hz wind speed, $U_{max,10}$, greater than 18 m/s;
- Gust factor, defined here as the ratio of the above 10-min maximum 1-Hz wind speed over the 10-min mean wind speed in the same interval, $G_{10} = U_{max,10}/\overline{U}_{10}$, greater than 1.5.

It is to be noted that the wind speed U here involved derives from the classical downburst decomposition technique (Section 3.1). According to the above procedure, the event is classified as a potential thunderstorm when at least one elevation AGL satisfies both the above conditions. Specifically, the fulfilment of the first condition links to the severity of the event recorded, while the latter implies that a short-time interval of high and off-mean wind speed has occurred during the 10-min observation which, therefore, might indicate the onset of thunderstorm winds.

Following this automated control, visual and qualitative inspections of the signals were carried out in order to verify whether they resembled the typical pattern of downburst time histories, where a sudden ramp-up of the velocity is followed by the related peak and dissipation stage. Finally, interpretations and cross-checking analyses with satellite and radar images, suitable to identify the height, shape and time evolution of the potential parent cloud, as well as with lightning occurrences were performed. Both the lightnings and the presence of high and spatially localized clouds, typical of cumulonimbus, may indeed confirm the thunderstorm nature of the event. This allowed to select and examine a subset of 10 downbursts over the whole dataset of events extracted with the automated procedure. The related parameters, shown in Table 1, are based on a time period $\Delta t = 10$ min, containing the development of the

Table 1
10 downburst events extracted: port, date and time of occurrence; maximum gust factor and its height, $G_{10_{max}}$ and $z(G_{10_{max}})$; maximum 1-Hz wind speed $U_{max,10}$ at the height $z(G_{10_{max}})$; absolute maximum 1-Hz wind speed $U_{max,10}$ and its height $z(U_{max,10})$; gust factor G_{10} at the height $z(U_{max,10})$.

Port	Date (YYYYMMDD)	Time (hh:mm) UTC	$G_{10_{max}}$	$z(G_{10_{max}})$(m)	$U_{max,10}$ (m/s) at $z(G_{10_{max}})$	$U_{max,10}$(m/s)	$z(U_{max,10})$(m)	G_{10} at $z(U_{max,10})$
GE	20150814	22:15	2.46	100	21.2	21.4	90	2.37
GE	20150815	19:55	2.53	200	24.9	31.8	60	1.84
GE	20160305	08:15	1.53	80	22.9	23.1	200	1.33
GE	20160503	18:15	2.87	80	21.3	24.3	140	2.82
GE	20180412	16:20	1.64	80	18.3	19.4	200	1.56
GE	20180513	18:40	1.59	180	19.0	19.0	180	1.59
LI	20150725	09:50	2.00	40	21.6	21.6	40	2.00
LI	20150913	11:10	2.26	120	26.3	26.3	120	2.26
LI	20151028	19:30	1.67	40	20.3	22.4	250	1.44
LI	20180604	10:10	1.65	250	18.8	19.4	100	1.53

storm, in agreement to the analytic criterion of extraction.

Fig. 3 depicts, at the height of $G_{10_{max}}$ defined in Table 1, the 20-min time histories of the slowly-varying mean wind speed $\overline{U}(t)$ (Eq. (2)) and direction $\overline{\alpha}(t)$ (Eq. (4)) for the 10 events extracted and classified as thunderstorms.

Table 2 reports, in a more quantitative form, the main meteorological information extracted from the related diagrams leading to the final definition of the subset of events. Based on the 1-h cumulative precipitation and on the definition given by Fujita and Wakimoto (1983), a downburst event is classified as wet when the cumulative precipitation is greater than 0.01 inch/h = 0.254 mm/h. The information on the cumulative precipitations were collected in the stations of Madonna delle Grazie (Genoa) and Stagno (Livorno), located approximately 3.15 km north-west and 7.10 km north-east in respect to the LiDARs in the port of Genoa and Livorno, respectively.

Hereafter, each downburst signal and the related statistical parameters will be evaluated over the time interval $\Delta t = 20$ min, centered on the occurrence of the peak wind speed at the height of occurrence of $G_{10_{max}}$. This assumption, which is usually disregarded in literature, where the investigation of the signal is performed over the period $\Delta t = 10$ min, was herein adopted with the aim of including the whole downburst-related part of the signal in the analysis. According with the different characteristics and durations of the downbursts here investigated, the 20-min time interval was found suitable to statistically address all of them.

4. The thunderstorm event on September 13, 2015

This section describes in detail the thunderstorm that occurred in Livorno on September 13, 2015 at about 11:00 UTC. Section 4.1 provides the meteorological scenario that triggered the formation of the downburst. Section 4.2 gives a first feedback on the wind speed and direction measurements during the event as acquired by the LiDAR and the anemometers. Section 4.3 applies the two decomposition techniques (Sections 3.1 and 3.2) to the signals recorded along the measurement heights. The wind speed and direction vertical profiles are critically interpreted in Section 4.4, whereas those related to the turbulence intensity are described in Section 4.5.

4.1. Meteorological scenario

On September 13, 2015, a deep Atlantic surface low pressure system moved to the south-west of Ireland. Meanwhile, a pronounced trough aloft extended its axis southward to Spain. During the day, the low-pressure system deepened and the movement of the narrow sector of warm and humid air of subtropical origin, which extended southward along the Mediterranean, induced south-westerly winds that triggered instability over northern and central Italy.

In the morning of 13 September, a deep convective system, which had formed over the Tyrrhenian Sea between Corsica Island and Tuscany, landed in the area of Livorno.

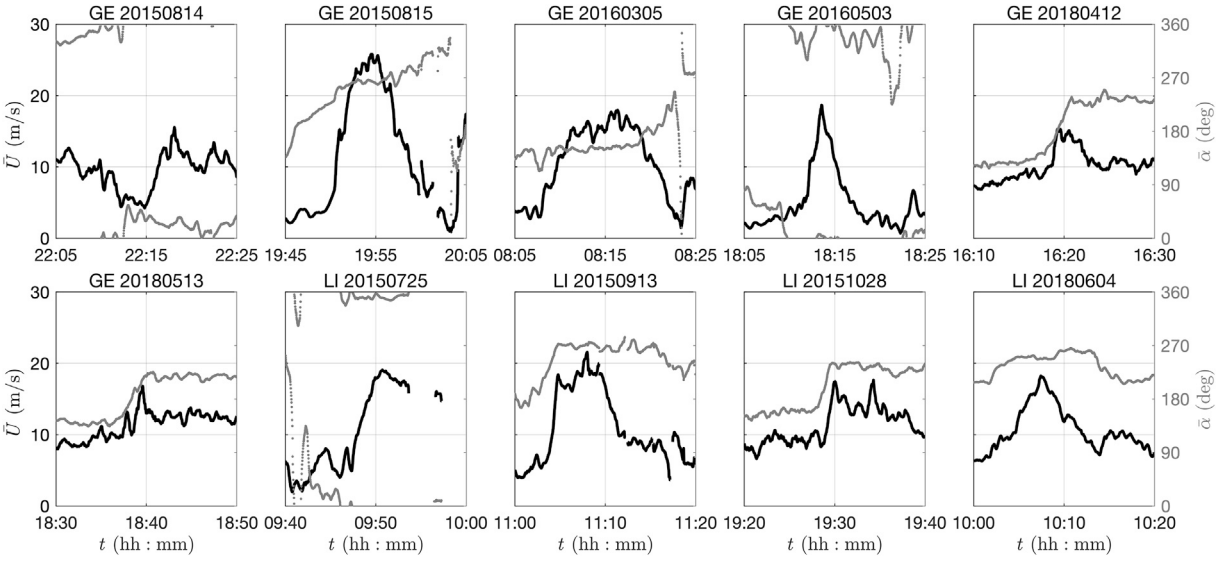

Fig. 3. 10 downburst events extracted: slowly-varying mean wind speed (black line) and direction (gray line) time histories. Event names are given in terms of station, SS, year, YYYY, month, MM, and day, DD.

Table 2
Main meteorological characteristics of the 10 downburst events according to radar (reflectivity [dBZ]), satellite (cloud top height [m]), lightning (strikes [Y/N]), and rain rate (ground cumulated precipitation [mm/h]) measurements, and corresponding downburst classification between wet and dry. Radar measurements were not available (NA) in 2015 in Livorno.

Port	Date (YYYYMMDD)	Time UTC	Reflectivity (dBZ)	h_{cloud} (km)	Lightnings (yes [Y], no [N])	1-h precipitation (mm/h)	Downburst type
GE	20150814	22:15	50	12	Y	13.4	Wet
GE	20150815	19:55	48	11	Y	5.4	Wet
GE	20160305	08:15	27	11.5	N	9.5	Wet
GE	20160503	18:15	22	7.5	N	0	Dry
GE	20180412	16:20	31	9	N	4.4	Wet
GE	20180513	18:40	24	9.5	N	3	Wet
LI	20150725	09:50	NA	15	Y	6.4	Wet
LI	20150913	11:10	NA	12.5	Y	14	Wet
LI	20151028	19:30	NA	12	Y	9.2	Wet
LI	20180604	10:10	18	12	Y	0	Dry

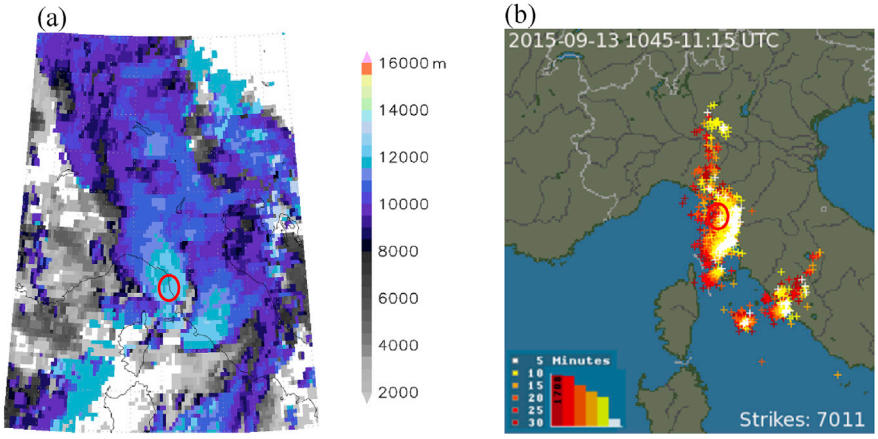

Fig. 4. (a) Cloud top height distribution from MSG data, acquired by Eumetsat and valid for September 13, 2015 at 11:00 UTC; (b) strikes recorded from 10:45 to 11:15 UTC on September 13, 2015 by means of Blitzortung network for lightning and thunderstorms, retrieved from the online archive. The red circles show the position of Livorno. (For interpretation of the references to color in this figure legend, the reader is referred to the Web version of this article.)

Panel (a) of Fig. 4 shows the distribution of cloud top heights obtained from the cloud analysis performed by Eumetsat, based on infrared measurements collected by SEVIRI on board the Meteosat Second Generation satellites. At 11:00 UTC, two different convective cells with cloud top height at more than 12,000 m approached the Italian coast, the northern one was exactly over Livorno (see red circle). The occurrence of these convective storms is confirmed by the intense lightning activity, which can be observed in Panel (b). From 10:45 to 11:15 UTC, the Blitzortung network recorded more than 7000 strikes overall. The strikes occurrence in time, defined by colors red to white, shows the northeastward movement of the storm.

4.2. LiDAR and anemometer measurements in the port of Livorno

At the time of the storm, the anemometers and the LiDAR in the port of Livorno recorded a sudden increase of the instantaneous horizontal wind speed $U(t)$ from about 6 to 26 m/s according to the LiDAR at 120 m AGL, which is the height where the maximum gust factor G_{10} along the whole profile occurred, and from 5 to 24 m/s according to the closest anemometer (LI.04, placed at 20 m above sea level). Contemporarily, the wind of both LiDAR and LI.04 veered about 100° from south-southeast to west-northwest during the ramp-up period and backed to the original direction after the wind speed returned to the previous low values. After the passage of the storm, in fact, the mobile mean wind speed and direction stabilised approximately to $\overline{U}(t) = 8$ m/s and $\overline{\alpha}(t) = 160$. This is captured in Fig. 5, showing the 1-h instantaneous horizontal wind speed and direction, as recorded by the LiDAR and anemometer LI.04, as well as their slowly-varying mean evaluated through a mobile time window $T = 30$ s. The classical decomposition method was invoked for the resultant mean wind speed $\overline{U}(t)$ (Eq. (2)), while the directional strategy was adopted for the mean wind direction $\overline{\alpha}(t)$ (Eq. (4)).

According to the LiDAR measurements, the 10-min maximum gust factor, over the whole profile, was 2.26 at 120 m AGL; at the same height, the 10-min mean wind speed was 11.7 m/s. However, the storm development lasted globally more than 10 min; the gust factor defined over 1 h at 120 m AGL was 3.29 as the 1-h mean wind speed was 8.0 m/s.

It is worth noting that the acquiring frequency of LiDAR and anemometers are different, i.e. 1 Hz and 10 Hz, respectively. As illustrated in Section 2, the LiDAR also measures the vertical component w of the velocity (Fig. 5 (a)), which may provide an information about the intensity of the downdraft stage of the storm when located within the measurement cone of the instrument. Non-zero values of this quantity, particularly closer to the ground, may also relate to the magnitude of the vertical component of the primary vortex embedded into the outflow.

4.3. Application of the classical and directional decomposition techniques

Fig. 6 shows the application of the classical downburst decomposition technique, described in Section 3.1, to four of the 12 measurement heights, i.e. $z = 50$, 100, 160 and 200 m; the rest of the heights are here not shown for sake of visualization. According to Zhang et al. (2019), high turbulence intensities (greater than 0.2) related to low slowly-varying mean wind velocities (below 5 m/s) were disregarded.

The maximum value of the slowly-varying mean wind velocity is $\overline{U}_{max} = 24.6$ m/s, recorded at the height $z = 180$ m AGL. The slowly-varying turbulence intensity has its maximum and minimum 20-min mean values respectively equal to $\overline{I}_{U_{max}} = 0.097$ at $z = 200$ m and $\overline{I}_{U_{min}} = 0.074$ at $z = 180$ m, while at the reference height of 120 m, $\overline{I}_U = 0.077$.

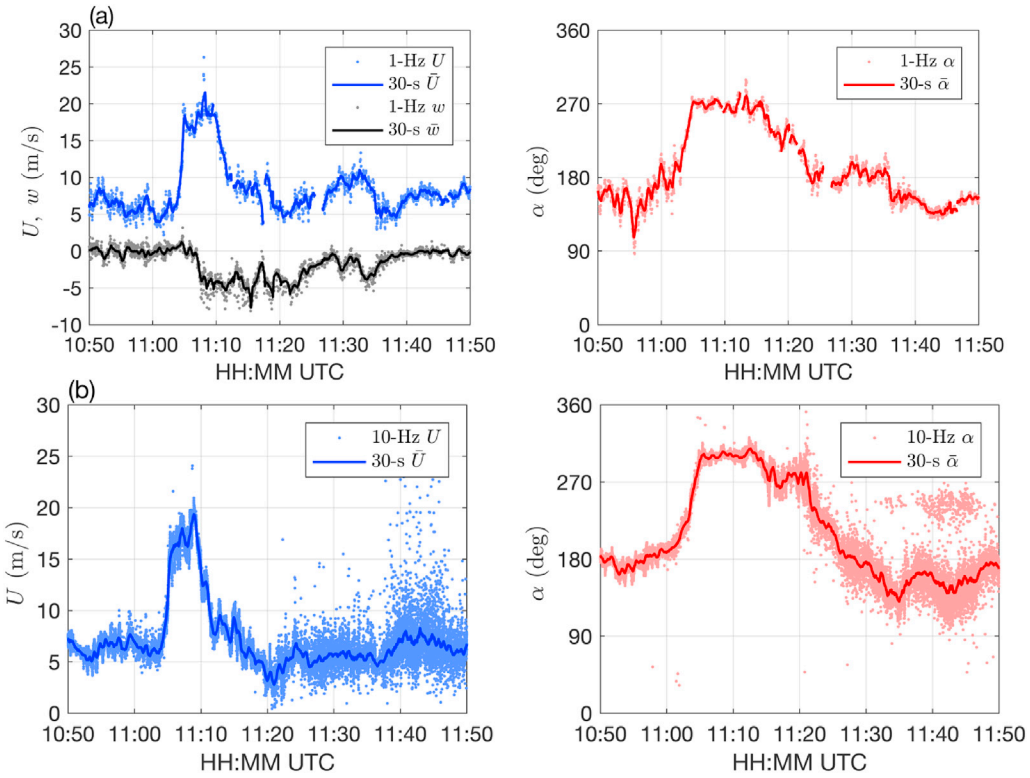

Fig. 5. (a) 1-h 1-Hz and 30-s mean horizontal and vertical wind speed and direction measurements recorded by the LiDAR at $z = 120$ m in the port of Livorno; (b) 1-h 10-Hz and 30-s mean wind speed and direction measurements recorded by the anemometer LI.04 at $z = 20$ m in the port of Livorno.

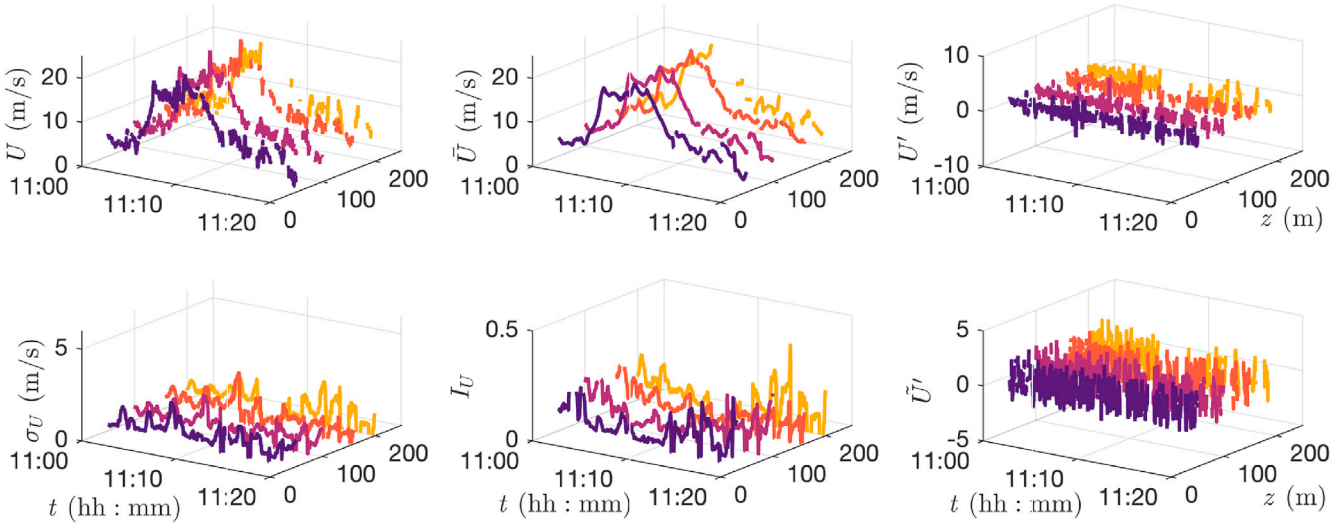

Fig. 6. Application of the classical decomposition (Section 3.1) to the downburst signal at $z = 50$, 100, 160 and 200 m.

The reduced turbulent fluctuation is characterised by near-zero mean and unit standard deviation throughout the elevation; the maximum and minimum values of its skewness are $\gamma_{U_{max}} = 0.126$ at $z = 100$ m and $\gamma_{U_{min}} = -0.246$ at $z = 180$ m, while those of kurtosis are $\kappa_{U_{max}} = 2.586$ at $z = 120$ m and $\kappa_{U_{min}} = 2.287$ at $z = 140$ m. At 120 m AGL, these parameters assume values $\gamma_U = 0.023$ and $\kappa_U = 2.586$. The average skewness and partly the kurtosis values are indeed in the neighborhood of the reference values associated to the Gaussian distribution, i.e. $\gamma = 0$ and $\kappa = 3$. However, the lower values of κ indicate a more flattened distribution with values more dispersed around the mean.

Fig. 7 shows part of the directional decomposition (Section 3.2) applied to the downburst outflow. The results are here shown only for $z = 120$ m, which is the height where the maximum value of G_{10} is observed.

The maximum value of the slowly-varying mean wind speed is $\overline{u}_{max} = 24.6$ m/s, recorded at $z = 180$ m, which exactly corresponds to the observed $\overline{U}_{max}$. Turbulence intensities show similar values in terms of longitudinal and lateral components which, in turn, are very close to the quantity referred to $\bar{I}_U$ (Section 3.1). At $z = 120$ m, where the maximum gust factor G_{10} is observed, $\bar{I}_u = 0.076$ and $\bar{I}_v = 0.082$, respectively, which are almost identical to the $\bar{I}_U = 0.077$ value evaluated for the resultant wind speed U by means of the classical decomposition technique; their ratio $\bar{I}_v/\bar{I}_u = 1.079$ is however greater than the reference

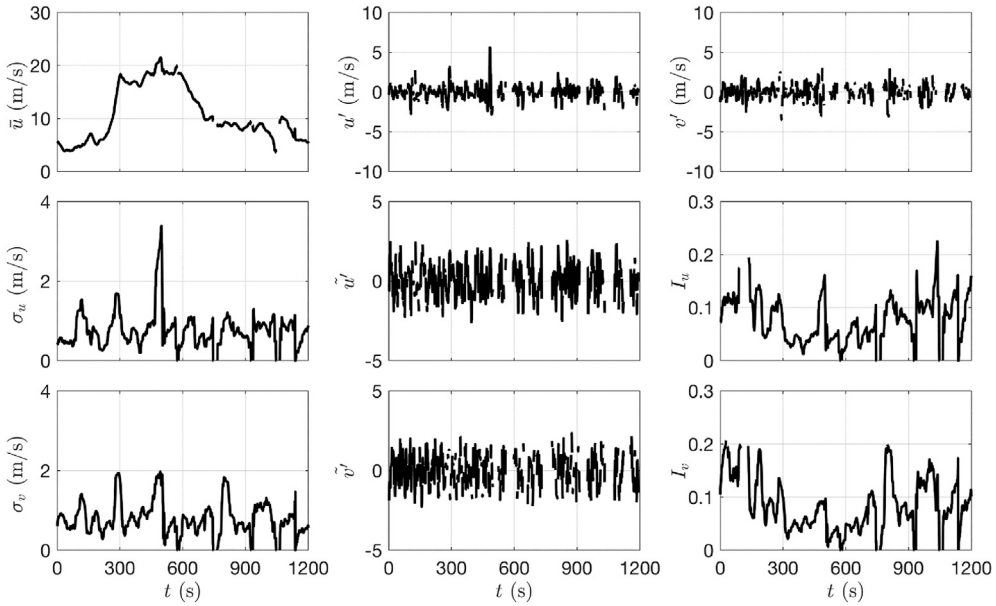

Fig. 7. Application of the directional decomposition (Section 3.2) to the downburst signal at $z = 120$ m.

value commonly adopted for synoptic winds in neutral conditions, $\bar{I}_v / \bar{I}_u = 0.75$ (Solari and Piccardo, 2001). The reduced turbulence components have again both fairly zero mean value and unit standard deviation along the height. At the reference height $z = 120$ m the skewness and kurtosis values are, respectively, $\gamma_u = 0.027$, $\gamma_v = -0.083$ and $\kappa_u = 2.559$, $\kappa_v = 2.219$. The longitudinal values of the skewness and kurtosis are found to closely match those obtained from the classical downburst decomposition at the same heights, with analogous considerations concerning their Gaussian properties also to extend to the lateral components.

4.4. Wind speed and direction vertical profiles

Fig. 8 shows the slowly-varying mean wind velocity (Eq. (2)) and direction (Eq. (4)) vertical profiles at 12 significant instants in the period

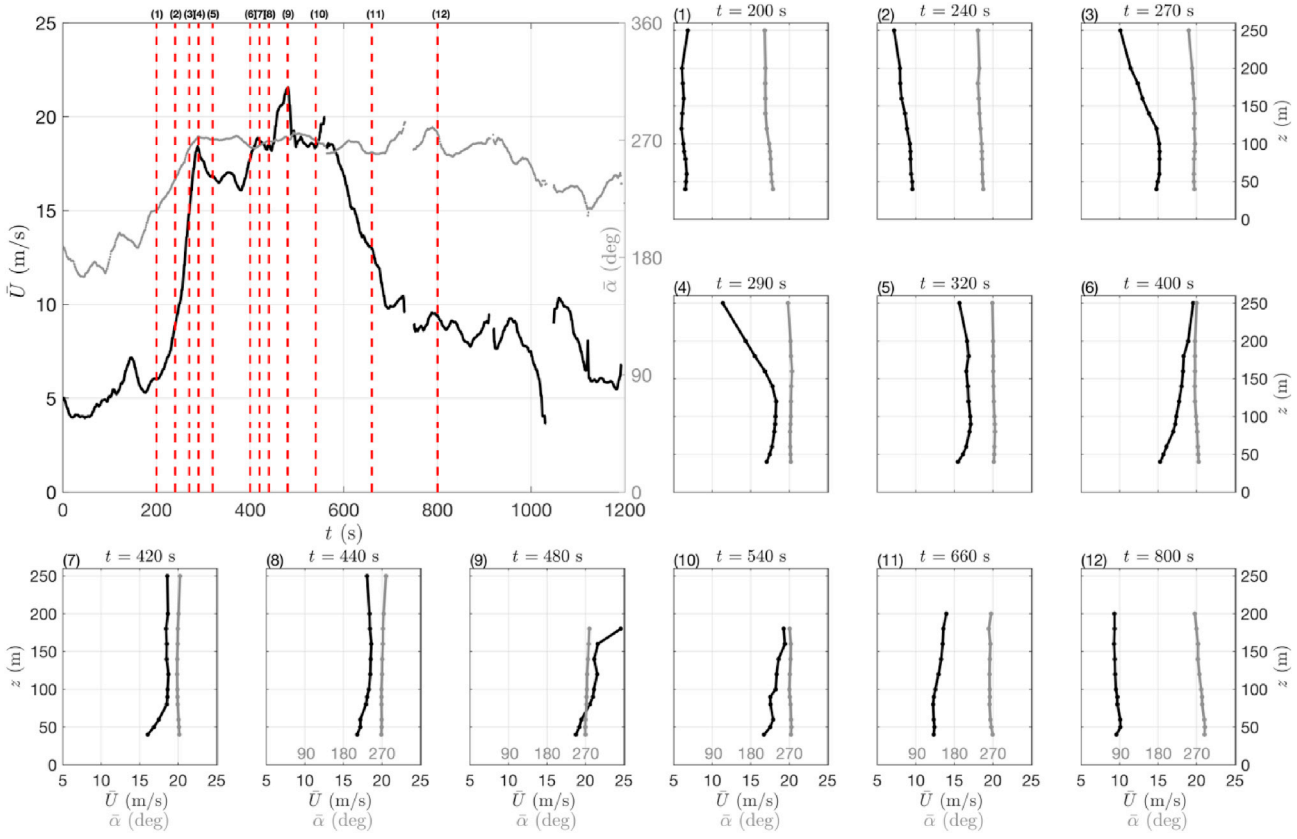

Fig. 8. Slowly-varying mean wind speed (black line) and direction (gray line): 20-min time-history at 120 m AGL (upper left-hand picture); vertical profiles at: 200, 240, 270, 290, 320, 400, 420, 440, 480, 540, 660 and 800 s (sub-boxes).

from 11:00 to 11:20 UTC (1200 s). The related time histories of $\overline{U}$(t) and $\overline{\alpha}(t)$ at 120 m AGL are shown in the upper-left box. Here, the velocity ramp-up lasts for approximately 75 s, i.e. from 215 to 290 s, with magnitudes from about $\overline{U} = 6$ m/s to the first peak, $\overline{U} = 18.3$ m/s. Meanwhile, the mean wind direction oscillates around $\overline{\alpha}(t) = 180°$ shortly before the storm occurrence and, concurrently with the wind speed ramp-up, it starts to veer clockwise from south to west. At $t = 290$ s, the direction settles to approximately 270° and remains fairly constant throughout the occurrence of the downburst. Similarly, the wind speed shows a plateau of roughly constant high wind speed in the range 15–18 m/s. The absolute peak mean wind speed $\overline{U}_{max} = 21.6$ m/s is reached at $t = 480$ s. At this moment, however, the absolute value is observed at the measurement height $z = 180$ m, where $\overline{U}_{max} = 24.6$ m/s (Fig. 8, Box 9). The wind speed likely continues to increase above this height forming a nose-shaped profile with tip higher in elevation, but the lack of records in the period of maximum intensity of the storm prevents to confirm such assumption.

Fig. 9 depicts the 10-min magnitude diagrams of the horizontal $\overline{U}(t)$ and vertical $\overline{w}(t)$ mean wind speed along with the mean wind direction $\overline{\alpha}(t)$, centered at the time of $\overline{U}_{max}$, as a function of time and height AGL.

Panel (a) of Fig. 9 shows the occurrence of the two observed velocity maxima in the time-space domain: the first appears very localized in time around $t = 290$ s with highest velocities in the range $z = 80$ m to $z = 120$ m; the second covers a wider time interval, starting 20 s before the time of the absolute peak, and spreads into a larger elevation range from $z =$ 60 m.

Fig. 9 (b) shows important aspects related to the vertical mean wind speed. Slightly before $t = 290$ s of the first peak of $\overline{U}(t)$, the little positive value of $\overline{w}(t)$ might be related to the upward vertical component of the primary vortex which has just impinged on the ground and is now leading the outflow. In agreement with the dynamics of the vortex itself, the maximum positive values are observed higher in elevation and few seconds before those related to the horizontal component of the wind speed. This scenario is confirmed by the subsequent zero and little negative $\overline{w}$ values, respectively concurrent with the maximum $\overline{U}$ and with the back-downward component of the vortex. At the time of the absolute peak of $\overline{U}$, the negative-sign intensification of $\overline{w}$ for high elevations suggests that the storm is passing over the instrument. This seems to be confirmed by the missing measurements above 160–180 m AGL, likely due to the heavy rain which characterizes the spatial region defined by the downdraft. Large negative vertical velocities of about 6–8 m/s are found for heights $z \geq 160$ m while, going down in elevation, the magnitudes are reasonably lower as streamlines have to spread horizontally at the ground.

To comprehend better what we are referring to in relation to the dynamics of the phenomenon, Fig. 10 depicts the flow visualization of a generic physical reproduction of a downburst at the WindEEE Dome. Based on the location of the measuring instrument, five main different situations can be identified in the outflow dynamics, as schematically shown by white arrows. With reference to the figure and to the downburst event herein analysed, the LiDAR's location allows, firstly, the recording of (1), (2) and (3) defining the first peak of the horizontal wind speed and, secondly, the passage of the downdraft over the instrument which is captured in the scenarios (4) and (5).

After the occurrence of the absolute peak, the horizontal velocity $\overline{U}$ in Fig. 9 (a) shows a second plateau of magnitude approximately 18.5 m/s, higher in respect to the previous stage of roughly constant velocity between the two peaks. After about 80 s, at $t = 560$ s, the descending part of the signal takes place. At $t = 750$ s, eventually, the velocity returns to low values of approximately $\overline{U} = 8$ m/s. Nevertheless, the vertical wind speed $\overline{w}(t)$ is observed to be still negative. The mean wind direction $\overline{\alpha}(t)$, instead, maintains the direction west-to-east for approximately 10 min and only at $t = 920$ s starts to veer anticlockwise towards the original south direction.

According to the boxes of Fig. 8, the velocity nose-like profile appears only in discrete portions before and eventually during the peaks. The colormap of Fig. 9 allows the analysis of the real duration of the nose shape profiles: it is clear in the final part of the ramp-up period, where the maximum velocity is experienced in the elevation range between 80 and

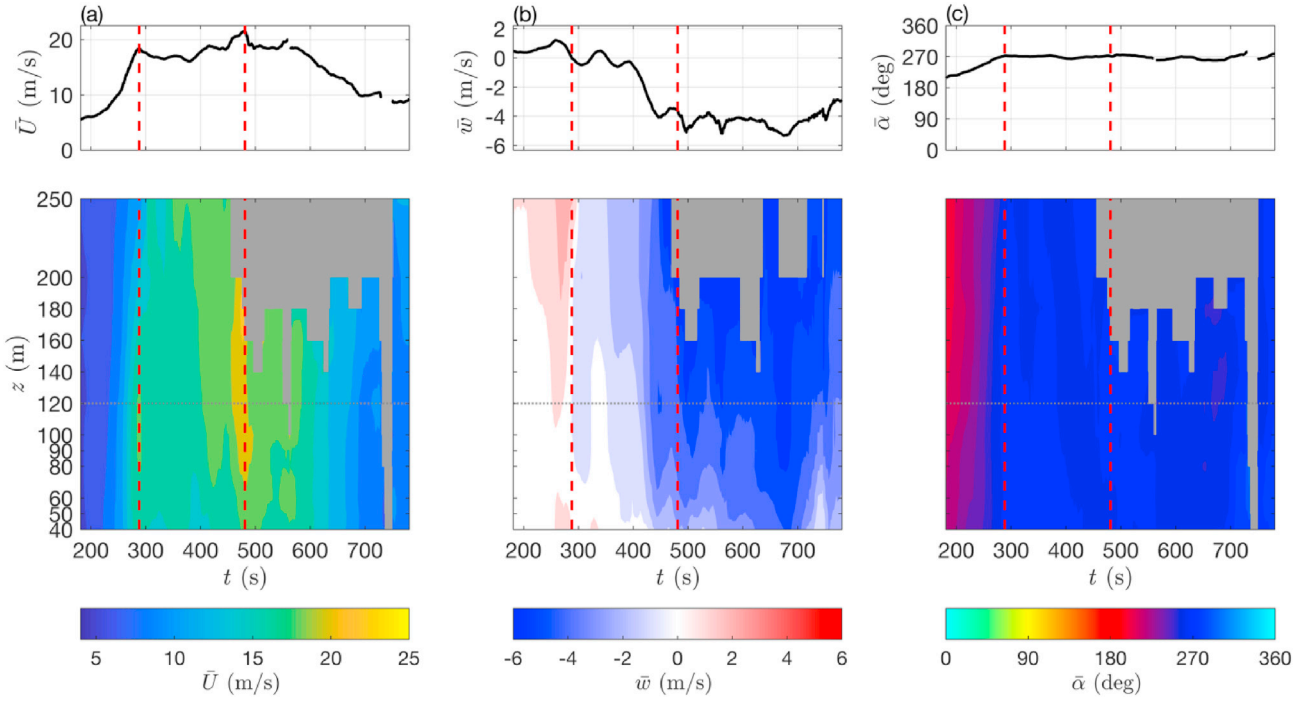

Fig. 9. 10-min horizontal (a) and vertical (b) slowly-varying mean wind speed; 10-min slowly-varying mean wind direction (c). Time histories at 120 m AGL (upper pictures); interpolated magnitude-maps as function of time and height (bottom pictures). Vertical dashed red lines indicate the time of the first and second peak of the horizontal mean wind speed. Horizontal dotted gray lines (bottom pictures) indicate the height at which the time histories are depicted (upper pictures). (For interpretation of the references to color in this figure legend, the reader is referred to the Web version of this article.)

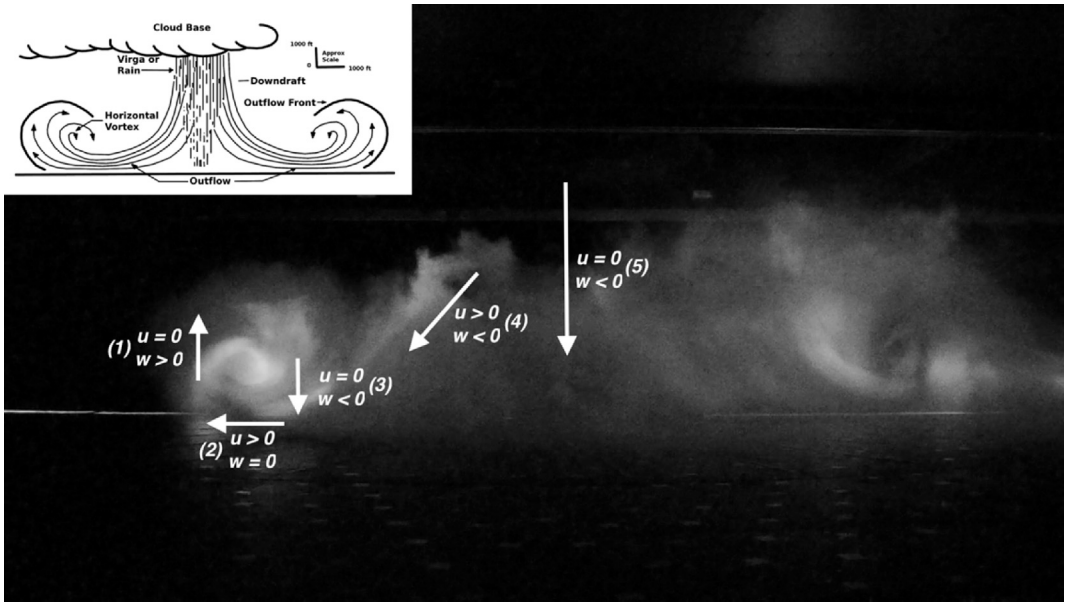

Fig. 10. Flow visualization with smoke of a downburst experiment at the WindEEE Dome. Scenarios (1) to (5) identify the main steps of the outflow dynamics. Schematic of the downburst dynamics (top-left picture, created by Federal Aviation Administration of United States).

120 m AGL and lasts from 260 to 325 s; it appears, less clearly, in the plateau interval before the second peak from 375 to 460 s in a somewhat spread range of altitudes (90–180 m AGL). In this latter interval, in fact, the maximum of the nose occurs at the highest elevations at $t = 380$ s, while it decreases to $z = 60$ m at $t = 425$ s. The velocity remains approximately constant above this height and up to the occurrence of the absolute peak. In the other parts of the ramp-up and in the post-peak period, the horizontal mean wind speed can be considered as almost constant or increasing with height. The nose-like shape, in the region of major evidence, disappears at 330 s lasting in total 65 s. The maximum velocity occurs at 480 s when the nose has already disappeared.

The wind direction $\overline{\alpha}(t)$ is observed to maintain a constant trend along the height throughout the downburst occurrence in Fig. 9 (c). The full scale investigation by Hjelmfelt (1988) and Wakimoto (1982) reported an average outflow depth of about 1.4 km, or even larger, with the vortex center located in the range 700–800 m AGL. It follows that the LiDAR's vertical range of measurements only covers the lower portion of the gust front outflow and below it, where the dominant flow component is the radial (scenario (2) of Fig. 10); for this reason, the direction is here observed to remain constant throughout the inspected heights. Since the same situation occurs for all the thunderstorms analysed here (Section 5.2), it represents a crucial finding and signature of the outflow vertical profile of thunderstorm winds, with highly relevant implications to the wind loading on structures: the wind direction can be assumed as

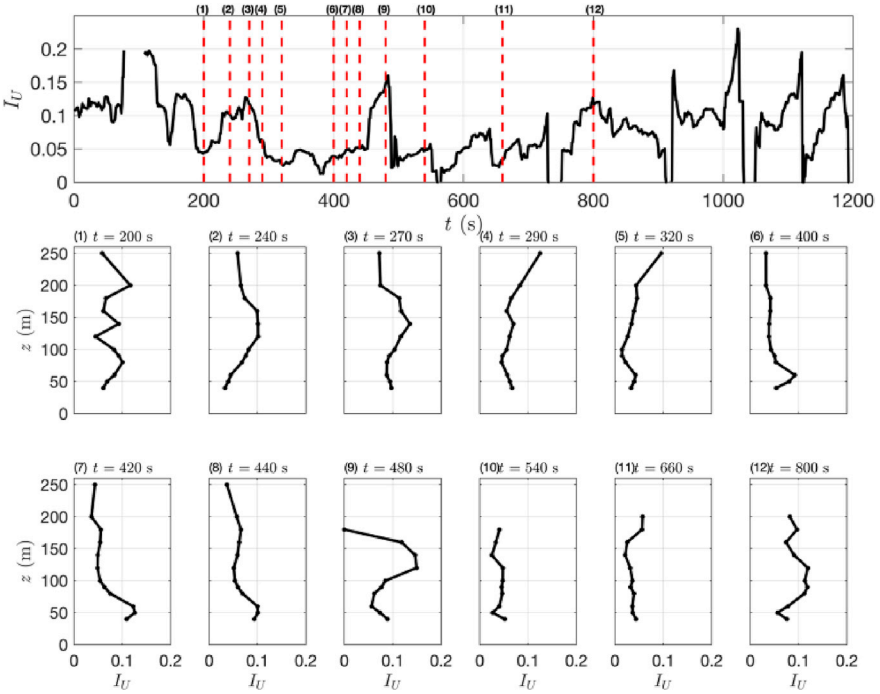

Fig. 11. Slowly-varying turbulence intensity: 20-min time-history at 120 m AGL (upper picture); vertical profile at: 200, 240, 270, 290, 320, 400, 420, 440, 480, 540, 660 and 800 s (sub-boxes).

invariant with height. By examining Fig. 8 and Panel (c) of Fig. 9, however, slight exceptions are here observed during the ramp-up stage of the velocity and simultaneous rotation of the direction where the wind seems to veer to west sooner at the lower heights. At the beginning of the ramp-up stage, $t = 200$ s, the approaching primary vortex pushes the ambient air outwards according to the outflow direction, likely forming a secondary and smaller vortex ahead of it. Consequently, the change in wind direction is sensed earlier at the lower heights: at 40 m and 250 m AGL $\overline{\alpha}$ is, respectively, 230° and 211°. With the occurrence of the first velocity peak 90 s later, at $t = 290$ s, the wind direction assumes a strong west component and the direction gap between the two heights is sharply reduced, $\overline{\alpha} = 272°$ and $\overline{\alpha} = 266°$, respectively.

4.5. Turbulence intensity vertical profile

Fig. 11 shows the vertical profile of the slowly-varying turbulence intensity (Section 3.1) at the same time frames considered in Fig. 8. Firstly, it is to be noted that the turbulence intensity magnitudes are all confined within $I_U = 0.23$, at least for the height $z = 120$ m shown in the upper panel. The height of maximum turbulence intensity seems to increase during the velocity ramp-up stage up to the top of the profile at the first peak, $t = 290$ s (Box 4). During the plateau part of the wind speed, instead, a clear nose-shaped profile appears at elevations 40–50 m AGL. At the time of the absolute peak velocity, $t = 480$ s (Box 9), the maximum value of $I_U = 0.149$ is found at $z = 120$ m. Later, its vertical trend does not appear to assume a recognizable behavior.

In analogy to Fig. 9, Fig. 12 shows the evolution of the slowly-varying standard deviation (a) and turbulence intensity (b) (Section 3.1) along the time and height AGL. The two parameters differ by a normalization factor $\overline{U}(t)$ in the evaluation of the non-dimensional quantity $I_U(t)$. Contrary to what assumed before, it is here decided to plot the entirety of values of I_U in order to obtain a more complete map, being aware that non-realistic high values might arise in correspondence of low $\overline{U}(t)$; the qualitative comparison with the graph of σ_U (Panel (b)) can overcome this issue. The two parameters assume an analogous general trend which, in the following, is discussed in relation to the behavior of $\overline{U}(t)$ (Fig. 9 (a)). The first peak in the velocity domain does not link with a simultaneous increase of I_U. In fact, a region of higher turbulence magnitude is observed approximately 25 s prior to the first velocity peak. Furthermore, such area is shifted at higher elevations in respect to the maximum $\overline{U}(t)$ in this stage. Analogous time-shift with the wind speed is observed in correspondence of the second maximum where, however, the turbulence intensity seems to occur at about the same height. In addition to that, about 60 s before the absolute peak of the mean wind velocity, I_U shows a localized region of rather high values at the lowest heights. Overall, the turbulence intensity maxima appear to precede the related wind speed peaks. This time-dependent behavior along the profile is observed in most events here analysed and will be discussed further in Section 5.3. The same concept is already found in Zhang et al. (2018b, 2019): by considering, respectively, 277 and 141 thunderstorm recordings, the ensemble mean of the parameter $\mu_U(t) = I_U(t)/\overline{I}_U$ shows a pronounced and off-mean spike few tens of seconds before the occurrence of the peak velocity. Our findings thoroughly mirror this situation. Its engineering implications in terms of wind loading and response of structures are not yet clear and out of the domain of this study, but surely represent an open topic which deserves future research.

5. Characteristics of the vertical wind profiles

This section provides a comprehensive discussion and comparison of the 10 downburst events extracted, in terms of vertical profiles of the slowly-varying mean wind speed (Section 5.1) and direction (Section 5.2) as well as the turbulence intensity (Section 5.3).

5.1. Slowly-varying mean wind speed

It is widely discussed by literature that, in the phase of maximum energy of the downburst, the outflow vertical profile assumes a typical nose-shaped form. In the mature stage of the phenomenon, the descending cold and dense column provokes high shear with the surrounding environment that triggers the formation of a vortex ring which, after its impingement on the ground, mightily spreads horizontally within a few hundred meters vertical layer. In this time frame, the maximum horizontal velocities are experienced at the boundary between the ground and the center of the vortex filament, usually in the range from 50 to 120 m AGL (e.g. Goff, 1976; Hjelmfelt, 1988; Lombardo et al., 2014).

In terms of mean wind speed signals $\overline{U}(t)$ (Eq. (2)), four of 10 downburst events are depicted in Figs. 13–16. Each of them shows the 10-min horizontal and vertical velocity time histories at the height of the maximum G_{10} (upper pictures) as well as the related magnitude maps (bottom pictures). Conventionally, the related diagrams are centered on the time of occurrence of the horizontal peak mean wind speed in the upper time histories ($t = 300$ s). Few investigated events show rather

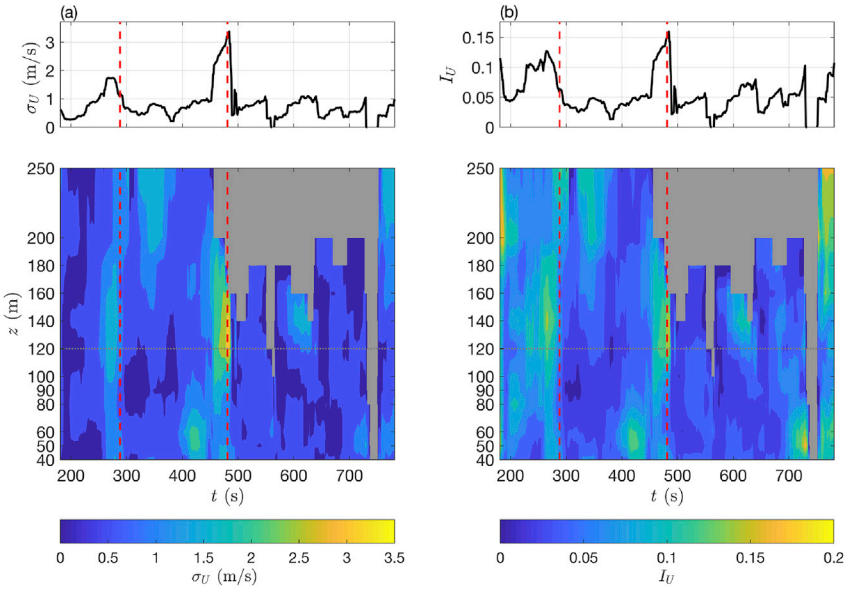

Fig. 12. 10-min slowly-varying standard deviation (a) and turbulence intensity (b): time histories at 120 m AGL (upper pictures); interpolated magnitude-maps as function of time and height (bottom pictures). Vertical dashed red lines indicate the time of the first and second peak of the horizontal mean wind speed. Horizontal dotted gray lines (bottom pictures) indicate the height at which the time histories are depicted (upper pictures). (For interpretation of the references to color in this figure legend, the reader is referred to the Web version of this article.)

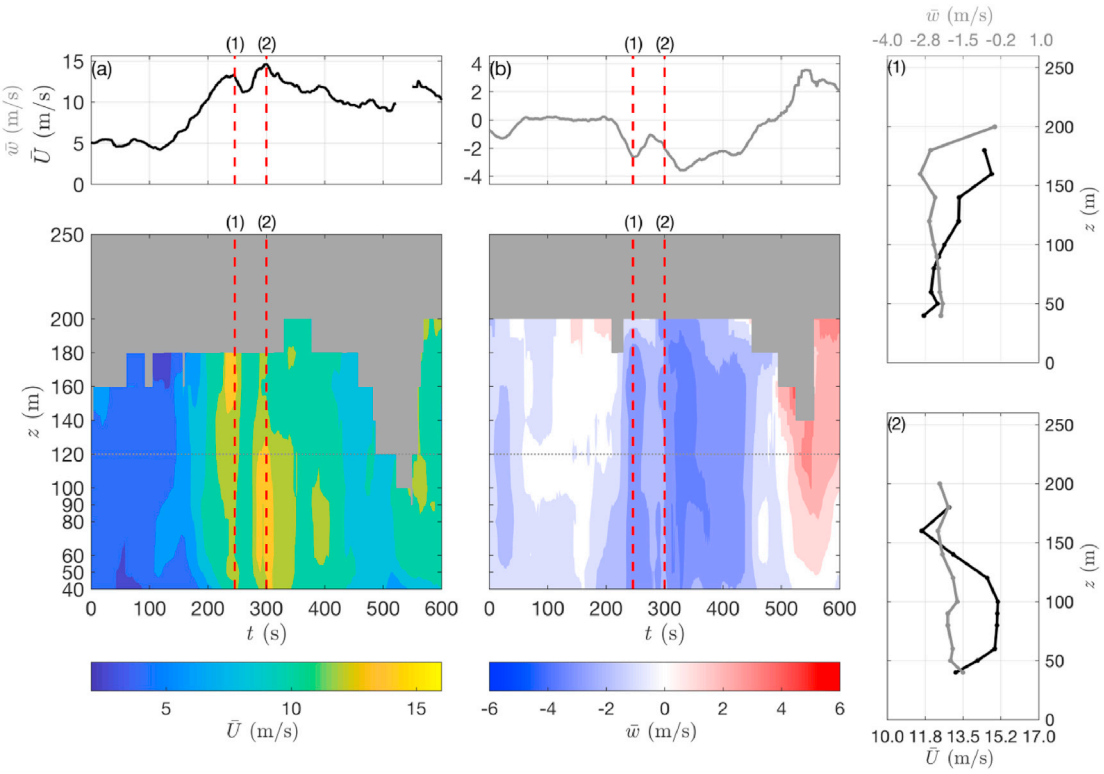

Fig. 13. Downburst in Genoa on August 14, 2015. 10-min horizontal (a) and vertical (b) slowly-varying mean wind speed: time histories (upper pictures); interpolated magnitude-maps as function of time and height (bottom pictures). Vertical dashed red lines indicate the time of the horizontal peak mean wind speeds, at which the vertical profiles of the horizontal and vertical slowly-varying mean wind speed are depicted (right-hand boxes). Horizontal dotted gray lines (bottom pictures) indicate the height at which the time histories are plotted (upper pictures). (For interpretation of the references to color in this figure legend, the reader is referred to the Web version of this article.)

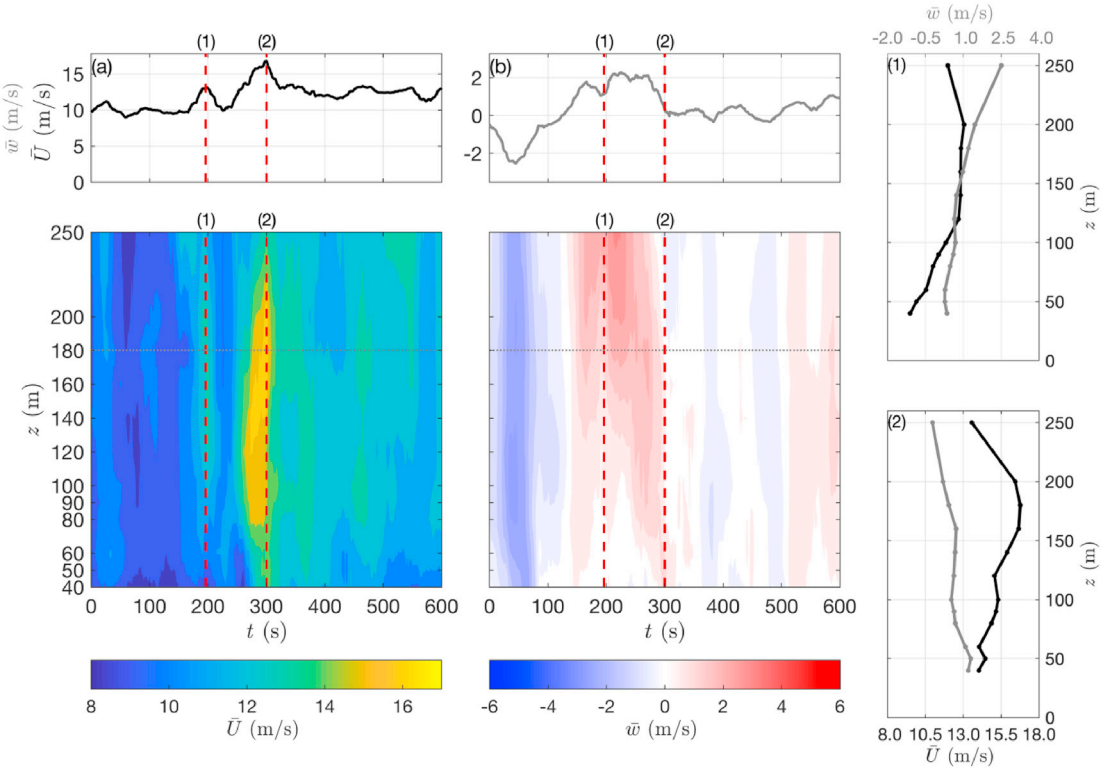

Fig. 14. Same as Fig. 13, but for the downburst in Genoa on May 13, 2018.

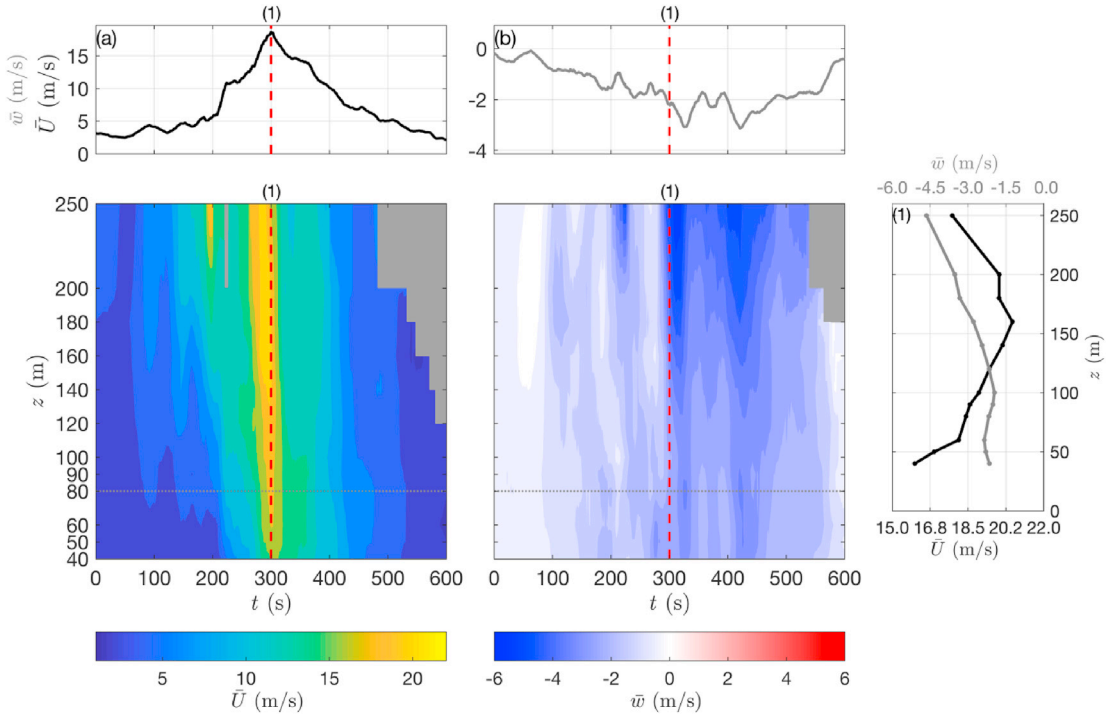

Fig. 15. Same as Fig. 13, but for the downburst in Genoa on May 3, 2016.

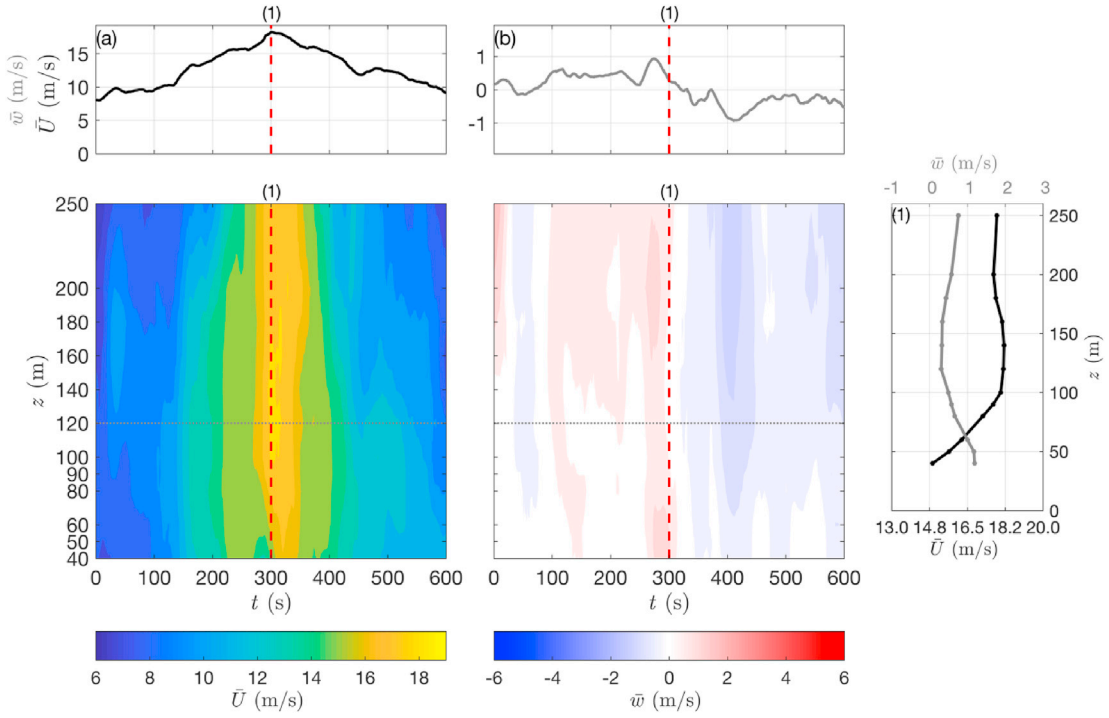

Fig. 16. Same as Fig. 13, but for the downburst in Livorno on June 4, 2018.

similar characteristics in respect to the downburst that struck Livorno on September 13, 2015 (Section 4.4). Two distinguished velocity maxima, of about the same magnitude, are observed in the event recorded in Genoa on August 14, 2015 (Fig. 13). Both the upper and bottom pictures of Panel (a) show that the horizontal mean wind speed, after a 130-s ramp-up stage, reaches the first peak $\overline{U} = 15.1$ m/s at $t = 245$ s and elevations above 140 m. The lack of data, however, does not allow to confirm whether the velocity above 160 m decreases, as it may appear in the black line in Box (1) of Fig. 13, which represents the vertical profile of the horizontal mean wind speed. Around 300 s, which is about 1 min after the first peak, a second peak occurs, but the height of the maximum wind speed is now shifted down to the range 40–120 m AGL. As highlighted in Box (2), the velocity profile here settles to a maximum value of $\overline{U} = 15.2$ m/s in the range 60–100 m AGL and then decreases quite rapidly until $z = 160$ m. A third, less intense, local maximum occurs around 400 s again in the range between 60 and 100 m AGL (Fig. 13 (a),

bottom picture). All these maxima correspond to vertical profiles of the horizontal mean wind speed with a clear nose-like shape, which comes and goes three times during the whole thunderstorm record. A quite strong downward flow component (Panel (b)) is observed during the time frames affected by high values of the horizontal wind speed. Both boxes (1) and (2) show values of the vertical component around −3 and −2 m/s at the first and second peak occurrence, respectively. Two aspects of these profiles are worth noting: first, the vertical profile in Box (1) shows a significant reduction of the vertical intensity at $z = 200$ m; second, in both profiles, $\overline{w}$ decreases from 200 to 40 m AGL, as expected because of the constraint $\overline{w} = 0$ at the ground. Also interestingly, the horizontal and vertical components of the wind speed seem to assume a quite correlated behavior, as it can be clearly noticed that the maximum negative vertical mean component occurs immediately after both the first and second maximum horizontal mean wind speed (see the red dashed lines (1) and (2) in Fig. 13 for reference). In an attempt to speculate about the physical meaning of the measurements described so far, we suggest that the first peak of $\overline{U}$, followed by the first minimum of $\overline{w}$, is related to the passage of the vortex ring above the LiDAR, which is always the first signature of a thunderstorm outflow. The earlier positive values of $\overline{w}$ above 180 m, cut off by the lack of data at the top of the profile, seem to confirm the situation depicted in the scenarios (1) to (3) of Fig. 10. Then, the second peak of $\overline{U}$, followed by the second minimum of $\overline{w}$, might be the footprint of the downdraft ((4) and (5), Fig. 10). This description seems to be consistent with the profile of the vertical velocity in Box (1) which sharply reduces to almost zero at 200 m AGL and therefore can be hardly associated to the downdraft. Conversely, in the profile in Box (2) the vertical component remains always negative as expected in case of the downdraft.

Similar considerations in terms of horizontal wind speed can be expressed for the thunderstorm event recorded on May 13, 2018 still in the port of Genoa (Fig. 14). Here, however, the time gap between the two peaks is about 100 s and the magnitude of the first appears approximately 3 m/s lower in respect to the absolute maximum. Both peaks occur at elevations above 120 m: at $t = 195$ s, depicted in Box (1), the velocity maintains a constant value of approximately $\overline{U} = 13.0$ m/s from $z = 120$ m to $z = 200$ m; at the time of the absolute peak (Box (2)), the horizontal wind speed increases up to 160 m AGL and, after a 40-m high plateau, decreases significantly to the top measurement height. Therefore, once again, it is confirmed that nose-like shape profiles occur concurrently with the maxima of the horizontal mean wind speed. Contrary to the event previously analysed, no relevant negative vertical velocity is measured during the whole thunderstorm, likely because the downdraft does not really pass over the LiDAR. Even more noteworthy, the vertical velocity increases between the occurrences of the two peaks and assumes positive values up to 3.0 m/s at the top of the profile (Fig. 14 (b), bottom picture). Following the same considerations addressed to the downburst LI29150913 (Section 4.4), this may be related to the passage of a vortex, which is supposed to be the primary vortex ring produced by the downdraft. Indeed, the LiDAR measures firstly the upward positive component in the leading part of the vortex and, secondly, the maximum horizontal wind speed which occurs closer to the ground at the bottom of the swirling structure; the subsequent slightly negative values of $\overline{w}$ at the top heights confirm this hypothesis (situation (1) to (3), Fig. 10). If this is the case, the first peak would be related to the secondary vortex which, as mentioned above, is sometimes produced ahead of the primary vortex ring when air is pushed outwards by the vortex expansion at the ground.

The other analysed events show more regular features, in the sense that the wind speed ramp-up and the ramp-down stages are of comparable duration and defined by the occurrence of a unique and clear peak. The storm recorded in Genoa on May 3, 2016 (Fig. 15) is characterized by an area of maximum intensities above 140 m which lasts for about 30 s. At the time of occurrence of the maximum velocity at $z = z(G_{10_{max}})$, a nose-shaped profile with tip at 160 m AGL is observed. Likewise most cases here investigated, a strong downdraft stream, clear above 200 m AGL, is observed slightly later than the occurrence of the maximum horizontal wind speed. This is believed to link with the passage of the storm over the measuring instrument when the downdraft touchdown is not far from the instrument itself, so that the primary vortex ring and the impinging jet-like phase cannot be clearly distinguished in the measurements (scenario (4) and (5), Fig. 10).

The downburst that occurred in Livorno on June 4, 2018 (Fig. 16) shows, again, a unique velocity peak. This is, however, contoured by smooth and slow-time stages of increasing and reduction of the wind speed. The highest magnitudes of about 18.2 m/s are experienced in the range of heights from 100 to 160 m AGL. The roughly uniform trend above the height of maximum wind speed has been observed also in other two events here not reported and is recorded in quite many studies in literature (Orwig and Schroeder, 2007; Ponte and Riera, 2007; Durañona et al., 2007; Holmes et al., 2008), even if a widely accepted explanation for that is not available. However, we may hypothesize that this situation happens when the vortex travels higher on the ground and thus the maximum horizontal velocities, occurring underneath the vortex itself, develop over a larger vertical extension. In the latter event shown, the vertical velocity does not record very negative values, but a rapid change of sign occurs exactly at the time of the peak, when the vertical velocity switches from positive to negative values. This seems related to the passage of a primary vortex ring when its shape is still quite symmetric, which means that the touchdown position is not very far from the instrument (scenario (1) to (3), Fig. 10). Moreover, as the upward and downward velocities $\overline{w}$ are in the order of 1 m/s, which is a rather low value, the core of the vortex was probably pretty much higher than 250 m AGL, which would confirm the assumption above. Finally, after 2–3 min from the peak $\overline{w}$ is zero again, so that it seems likely that the instrument was not affected by the impinging jet-like flow of the thunderstorm downdraft.

Table 3 shows the main parameters describing the slowly-varying mean part of each outflow signal here investigated, with particular regard to their vertical profiles.

Fig. 10 clarifies the nature of the observed positive and negative vertical velocities. The strongest negative values of the vertical mean wind speed $\overline{w}$ are likely to be related to the downdraft component of the storm (see (4) and (5), Fig. 10). In this situation, the instrument is located within the idealized cone defined by the descending and vigorous flow towards the ground. Indeed, Table 3 shows that the maximum negative values of $\overline{w}$ are often acquired at the top of the profile measured by the LiDAR, around 200–250 m AGL. On the other hand, low or even positive values of this quantity imply that the touchdown position of the storm is further away from the location of the instrument. Lower negative and positive values can, however, be due respectively to the back-downward and front-upward components of the vortex ring during its passage over the instrument (see (1) and (3), Fig. 10).

5.2. Slowly-varying mean wind direction

One of the main advantages of the new decomposition strategy is the ability to extract the time-dependent slowly-varying wind direction $\overline{\alpha}$ or $\overline{\beta}$ (Section 3.2), which is thus dealt within the wind velocity model itself. This allows to overcome the drawbacks of the classical rule, where the wind direction is considered only qualitatively but, eventually, disregarded in quantitative terms.

During the occurrence of thunderstorm outflows, the wind direction is usually observed to veer significantly with respect to the direction of the background wind – namely the synoptic wind in which the downburst embeds into. In agreement with literature, Fig. 3 (Section 3.3) has pointed out the following relevant aspect: the sudden change in the slowly-varying mean wind direction often occurs in correspondence of the simultaneous increase of the wind speed prior to the occurrence of the peak. The wind direction recorded by the measuring instrument corresponds, at first, with that of the background wind in the boundary

Table 3
Main characteristics of the nose-shaped profiles: maximum horizontal mean wind speed along the profile and its height, $\overline{U}_{max}$ and $z(\overline{U}_{max})$; vertical mean wind speed $\overline{w}$ at the time and height of $\overline{U}_{max}$; range of heights of the nose and its duration, h_{nose} and T_{nose}; maximum negative vertical mean wind speed and its height, $\overline{w}_{max}(-)$ and $z(\overline{w}_{\max(-)})$; maximum positive vertical mean wind speed and its height, $\overline{w}_{max}(+)$ and $z(\overline{w}_{\max(+)})$. Event names are given in terms of station, SS, year, YYYY, month, MM, and day, DD.

port_date	$\overline{U}_{max}$ (m/s)	$z(\overline{U}_{max})$ (m)	$\overline{w}$ (m/s)	h_{nose} (m)	T_{nose} (s)	$\overline{w}_{max}(-)$ (m/s)	$z(\overline{w}_{\max(-)})$ (m)	$\overline{w}_{max}(+)$ (m/s)	$z(\overline{w}_{\max(+)})$ (m)
GE20150814	15.7	60	−2.0	80–100	70	−3.6	120	2.4	200
GE20150815	28.4	180	−7.4	100	25	−11.5	200	2.4	180
GE20160305	20.4	200	−0.1	140–160	30	−0.8	100	3.1	250
GE20160503	21.7	160	−1.8	140–160	30	−5.4	250	0.8	160
GE20180412	16.9	200	0.4	80–100	25	−0.8	80	3.5	200
GE20180513	16.8	180	0.3	140–160	30	−2.6	100	3.1	250
LI20150725	19.8	200	−0.8	100–120	60	−2.5	80	1.1	200
LI20150913	24.6	180	−5.0	90–120	70	−8.7	200	1.1	40
LI20151028	21.8	250	−3.5	50–100	50	−6.8	200	4.2	250
LI20180604	18.2	120	0.3	100–180	35	−1.3	200	1.5	40

layer; subsequently, the embedded outflow provokes the direction to change accordingly to the position of the instrument in respect to the touchdown position. The translation of the thunderstorm cell plays, then, a significant role in the rate of this change.

Therefore, the main focus of this paragraph is to investigate the vertical variation of the mean wind direction along the profile recorded by the LiDAR. Fig. 17 shows, for the 10 downbursts examined, the maximum variation of the mean wind direction $\overline{\alpha}(t)$ among the sensed heights (black dotted line). This is computed for the 20-min time interval containing the peak wind velocity. The overlap with the wind speed time history (gray solid line) allows to draw some conclusions on the along-height change of the wind direction during the development of the storm.

Section 4 has described in detail the downburst event LI20150913. By considering the time instants highlighted by the vertical red lines of Fig. 8 and, even more intuitively, Panel (c) of Fig. 9, the maximum vertical variation of the mean wind direction is about 20° at the beginning of the velocity ramp-up stage (Box (1) of Fig. 8). However, Fig. 17 now points out that the direction varies up to $\Delta\overline{\alpha} \cong 40°$ prior to the embedment of the outflow into the background wind. Almost the entirety of the events studied here show a very similar behavior in this sense. Indeed, the direction along the profile is observed to largely vary prior to or at the very first stage of the velocity ramp-up. While increasing the wind speed, the vertical variation of the direction becomes smaller and smaller until the occurrence of the peak, where $\Delta\overline{\alpha}$ is at the minimum value, usually in the range 5–10°. Here the wind direction can be dealt with, to a very good extent, as constant along the vertical profile. This behavior is maintained throughout the peak interval while, during the velocity dissipation phase, the vertical variation widens again visibly; in the very last part of the velocity ramp-down and later, $\Delta\overline{\alpha}$ is sometimes found to reach values of 80°.

Two events show slightly different behavior of this parameter. GE20180513 and LI20151028 respectively exhibit the maximum values $\Delta\overline{\alpha} = 24°$ and 41° only 15 s and 35 s prior to the peak velocity. In general, however, the wide vertical changes in direction are in correspondence of the background wind, in both pre- and post-outflow intervals. Upon the downdraft impingement on the ground, the vigorousness of the generated outflow overcomes the influence of the boundary layer flow and the wind direction measured by the instrument is actually the non-linear superposition of both flows.

5.3. Turbulence intensity

Fig. 18 shows the time-dependent variation along the height of the turbulence intensity I_U, evaluated by means of the classical method (Section 3.1), for the four events depicted in Section 5.1. It aims at providing a clear framework of the turbulence characteristics corresponding to the related slowly-varying mean wind speeds. The dimensional standard deviation σ_U (not shown here) has again provided an interpretation and double-check on the values assumed by the turbulence intensity.

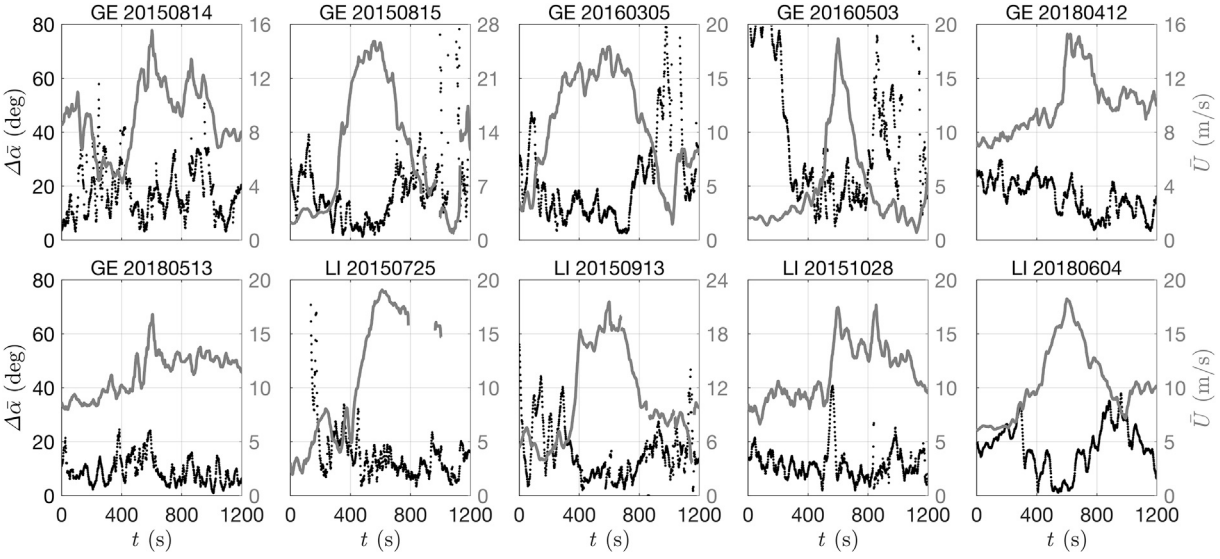

Fig. 17. 20-min evolution of the maximum along-height variation of the mean wind direction (black dotted line); 20-min time history of the mean wind speed (gray solid line) at $z = z(G_{10_{max}})$. Event names are given in terms of station, SS, year, YYYY, month, MM, and day, DD.

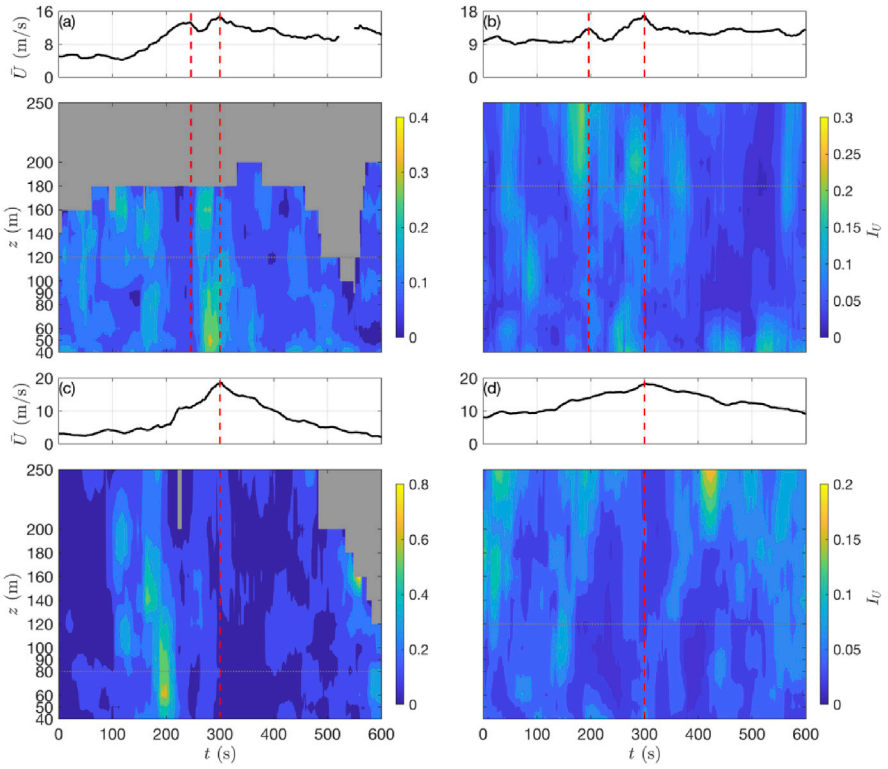

Fig. 18. Downburst events: Genoa on August 14, 2015 (a), May 13, 2018 (b) and May 3, 2016 (c); Livorno on June 4, 2018 (d). 10-min time histories of the horizontal slowly-varying mean wind speed at $z = z(G_{10_{max}})$ (upper pictures); interpolated magnitude-maps of the turbulence intensity I_U as function of time and height (bottom pictures). Vertical dashed red lines indicate the time of occurrence of the horizontal peak mean wind speeds. Horizontal dotted gray lines (bottom pictures) indicate the height at which the time histories are depicted (upper pictures). (For interpretation of the references to color in this figure legend, the reader is referred to the Web version of this article.)

At the beginning of the ramp-up phase of $\overline{U}$, the downburst recorded in Genoa on August 14, 2015 (Panel (a)) exhibits turbulence intensities in the order of $I_U = 0.25$ at $z = 160$ m. The same values of I_U are found in the middle of the velocity ramp throughout the whole vertical profile while about 40 s prior to the first velocity peak I_U assumes very low values tending to zero. Two localized maxima of the turbulence intensity are observed in between the two wind speed peaks. The first is observed at $t = 275$ s and $z = 160$ m; it appears with a time delay of approximately 25 s in respect to the first maximum in terms of horizontal velocity, and its height of occurrence suggests the correlation with this latter. About 5 s later, the second area of high off-mean values of $I_U = 0.38$ is observed at the location $z = 50$ m and few seconds earlier in respect to the high values of $\overline{U}$ defining the earlier boundary of the absolute peak velocity time interval. The maximum values of $\overline{U}$ at the second peak interval are, in fact, observed starting from a near-ground elevation up to about 120 m AGL. The elevation of both regions of local maxima of I_U seems to lie at the lower boundary of those related to the local maxima of $\overline{U}$.

Two confined areas of higher turbulence intensity ($I_U \cong 0.23$) are

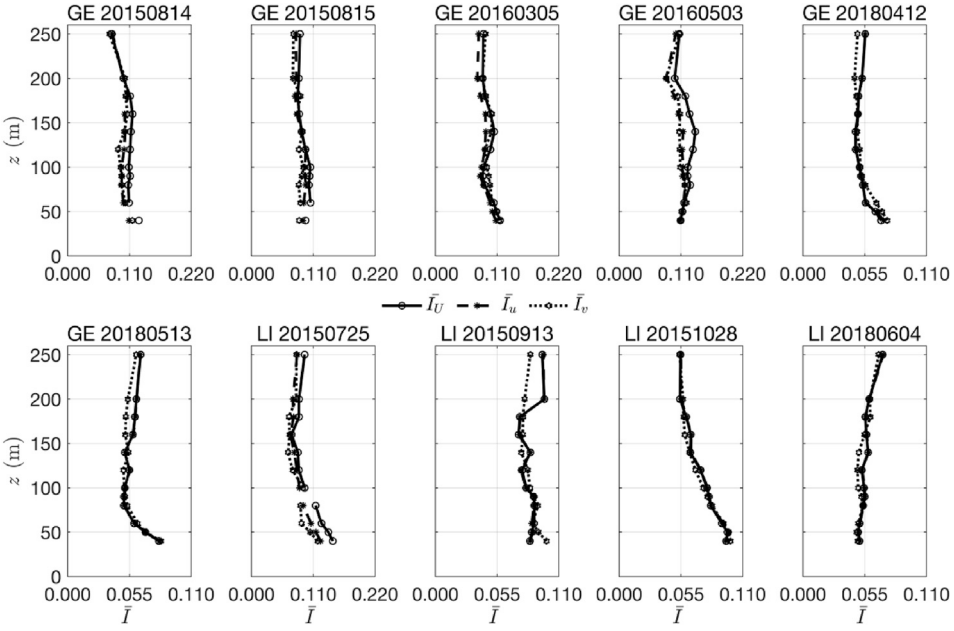

Fig. 19. Vertical profile of the 20-min mean slowly-varying turbulence intensity $\bar{I}_U$, $\bar{I}_u$ and $\bar{I}_v$. Event names are given in terms of station, SS, year, YYYY, month, MM, and day, DD.

observed also in the event shown in Panel (b). In this case, they are both slightly prior compared to the occurrences of the velocity peaks: the first is observed about 8 s earlier and few tens of meters higher, while the second, located at $z = 200$ m, occurs 15 s prior to that related to $\overline{U}$. The two areas seem now to seat at the top of those related to the high values of $\overline{U}$. The low magnitude of this latter parameter clearly causes the high values of I_U at the bottom of the profile at $t = 250$ s. The event occurred in Genoa on May 3, 2016 (Panel (c)) shows, at the beginning of the ramp-up stage of $\overline{U}$ ($t = 195$ s), an area of high localized $I_U \cong 0.7$ at $z = 60$ m. The thunderstorm in Livorno on June 4, 2018 presents very low values of the turbulence intensity throughout the time history. During the velocity ramp-up, the area defined by the iso-contour of $I_U \cong 0.12$ seems to shift to higher elevations by increasing $\overline{U}$. A peak of $I_U \cong 0.2$, confirmed by the analysis of σ_U, is surprisingly observed at the top elevation $z = 250$ m during the ramp-down of the mean wind speed.

Fig. 19 shows, for each of the 10 downburst events, the vertical profiles of the 20-min mean slowly-varying turbulence intensities evaluated through the classical method, I_U, and directional method, I_u and I_v.

Most events here analysed show the maximum 20-min mean value of the turbulence intensity at the bottom of the profile, $z = 40$ m, which decreases above following, however, different behaviors. At the top of the profile the turbulence intensity is usually observed to increase again. The occurrence of the maximum is observed in the mid-level profile, i.e. in the range 120–180 m AGL, only in the case of GE20160503.

As envisaged in Section 4, the longitudinal component of the turbulence intensity $\overline{I}_u$ assumes very similar, almost overlapping, values in respect to $\overline{I}_U$ referred to the resultant wind speed U. Little variations in this sense are observed only in the events GE20160305 and GE20160503, where $\overline{I}_u$ is slightly lower than $\overline{I}_U$ at elevations above 100 m, approximately. $\overline{I}_u$ appears lower throughout most of the profile in the event LI20150725. It is again highlighted the little detachment of $\overline{I}_v$ from both the previous profiles. In general terms, it appears shifted to slightly lower values in all events.

Table 4 reports, for each event, the average value over the measurement heights of the 20-min mean slowly-varying turbulence intensity – $\overline{I}_U$ (Section 3.1) and $\overline{I}_u$, $\overline{I}_v$ (Section 3.2) as well as of the skewness – γ_U and γ_u, γ_v, and kurtosis – κ_U and κ_u, κ_v of the reduced turbulent fluctuations along with their cross-correlation coefficient ρ_{uv}. It is worth reminding that the statistical parameters are obtained upon the use of a mobile averaging period $T = 30$ s to filter the signal.

The last two rows of the table show the ensemble values of the investigated parameters performed separately over the records in the ports of Genoa and Livorno. $\overline{I}_U$, $\overline{I}_u$ and $\overline{I}_v$ present very similar values: $\overline{I}_U$ is almost coincident or slightly greater than $\overline{I}_u$ which, in turn, results few thousandths greater than $\overline{I}_v$. Overall, these values result slightly lower but in general good agreement with the findings of Zhang et al. (2018b, 2019), where an extensive set of thunderstorm outflow records was extracted and analysed from ultrasonic measurements.

While the skewness values are all found to be very close to zero, with $\gamma_U = 0.083$ being the most detached value, κ is observed to be around 2.4 for all events. This result confirms the theoretical considerations provided by Tubino and Solari (2020); in this specific case they are strengthened by the capability of LiDAR to properly measure turbulence despite the Gaussian properties of $\tilde{U}'(t)$ are not entirely complied. Moreover, as remarked by Zhang et al. (2019) and in analogy to synoptic winds, the cross-correlation coefficient ρ_{uv} shows that the longitudinal and lateral reduced turbulence components can be dealt as un-correlated.

6. Conclusions and prospects

This paper provides a description and interpretation of the wind vertical profiles measured, by means of LiDAR wind profilers located in the Northern Mediterranean, during 10 thunderstorm events in the period 2015–2018. The events are selected through an automated procedure involving systematic quantitative controls of fixed thresholds of the 10-min maximum 1-Hz wind speed and gust factor. The actual nature of these events is checked with information such as satellite and radar images as well as lightning occurrences.

Overall, important aspects related to the mean (i.e. deterministic) part of the signal are found. Part of the events examined show a single maximum of the horizontal wind speed, whereas other events show two localized maxima. This characteristic can be referred to two different scenarios: in the case of LI20150913 (Section 4) and GE20150814 (Section 5), the LiDAR records first the travelling radial vortex and, afterwards, the passage of the downdraft over the instrument itself, producing two distinct peaks; in the event GE20180513 (Section 5), the first peak is likely to be related to the secondary vortex which is, few seconds later, followed by the primary one. The nose shape of the wind speed vertical profile is somewhat clear in all the downburst events here investigated; this is limited to quite short time intervals during the ramp-up and peak stages. The velocity is often found to assume a roughly constant value above the height of occurrence of the maximum, but the lack of data above 250 m AGL prevents to confirm such characteristic.

The analysis of the wind direction along the profile delivers a very important outcome: during the occurrence of the downburst, the direction is observed to be invariant with the height for all the events investigated. The strength of the outflow, generated by the impingement of the downdraft, suppresses the effects of the background wind.

The accuracy of LiDAR to measure turbulence components is discussed and the resulting values of each signal, cleaned from abnormal large values in correspondence of very low $\overline{U}$, are found to be in good agreement with those evaluated for a larger dataset of downburst outflows from ultrasonic measurements (Zhang et al., 2018b, 2019). It is proven that the quantities classically evaluated with reference to the resultant wind speed closely match those obtained through the directional decomposition rule,

Table 4
Along-height average value of: 20-min mean slowly-varying turbulence intensities $\overline{I}_U$, $\overline{I}_u$ and $\overline{I}_v$; skewness γ_U, γ_u and γ_v; kurtosis κ_U, κ_u and κ_v; cross-correlation coefficient ρ_{uv}. Event names are given in terms of station, SS, year, YYYY, month, MM, and day, DD.

port_date	$\overline{I}_U$	$\overline{I}_u$	$\overline{I}_v$	γ_U	γ_u	γ_v	κ_U	κ_u	κ_v	ρ_{uv}
GE20150814	0.108	0.099	0.098	0.028	0.027	0.045	2.357	2.342	2.478	−0.040
GE20150815	0.094	0.089	0.085	0.083	0.088	−0.035	2.472	2.435	2.423	0.024
GE20160305	0.095	0.088	0.097	−0.006	−0.002	−0.007	2.386	2.392	2.399	0.022
GE20160503	0.119	0.108	0.108	−0.025	0.003	0.004	2.462	2.481	2.468	0.001
GE20180412	0.054	0.054	0.055	−0.040	−0.036	0.050	2.422	2.422	2.555	−0.013
GE20180513	0.059	0.059	0.058	−0.034	−0.024	0.010	2.407	2.403	2.379	−0.074
LI20150725	0.102	0.089	0.084	0.008	0.022	−0.030	2.359	2.387	2.369	−0.001
LI20150913	0.085	0.085	0.085	−0.037	−0.033	−0.047	2.482	2.482	2.493	0.000
LI20151028	0.074	0.075	0.073	−0.063	−0.059	0.001	2.481	2.481	2.421	0.028
LI20180604	0.055	0.056	0.053	−0.003	0.001	0.004	2.379	2.375	2.419	−0.050
Ens. GE	0.088	0.083	0.083	0.001	0.009	0.011	2.418	2.413	2.451	−0.013
Ens. LI	0.079	0.076	0.074	−0.024	−0.017	−0.018	2.425	2.431	2.426	−0.006

especially with regard to the longitudinal component of the wind speed. However, also the lateral turbulence component is found to assume very similar values and only slightly lower.

The temporal analysis of the along-height behavior of the turbulence intensity I_U shows another relevant aspect: its highest values are usually found few tens of seconds prior to the occurrence of the horizontal peak wind speed. This reflects the findings of Zhang et al. (2018b, 2019) where a sharp increase of I_U was observed prior to the occurrence of the velocity peak on a large set of downbursts. This makes questionable the usual hypothesis adopted in literature, where $I_U=\bar{I}_U$, i.e. $\mu_U=1$. Research is still on-going to identify its implications in terms of structural loading and response. Besides this, in the present research we could not find a defined vertical behavior of the maximum values of I_U in respect to those of the horizontal wind speed.

A clear understanding of the evolution in time of the wind direction, as shown in Sections 4 and 5, is of crucial importance to fully comprehend the travelling nature of downbursts and the related impact on structures by analysing their behavior in terms of alongwind and crosswind response. Indeed, the systematic analysis of downburst vertical profiles is one of the main targets of the THUNDERR Project in order to clarify the time and height evolution of the mean and turbulent components of the signals. In this sense, a great and additional contribution to the WPS monitoring network has recently been given by the introduction of the new "Scanning WindCube" LiDAR, installed in the port of Genoa. It provides the reconstruction of the wind field on both the vertical and horizontal planes by taking advantage of a wide and deep scanning resolution. The complementary use of the "Scanning" and "Vertical Profiler" LiDARs will offer a full picture of the storm physical behavior, starting from tracking its propagation and core dimension at the near-ground region and, also, shedding new lights on the interplay of the outflow embedded in the background ABL wind and influenced by the thunderstorm cell translation. In this panorama and by looking at the project THUNDERR from a wider and general perspective, the physical investigation of such interactions in ad-hoc laboratories will provide a further and necessary step towards the detailed reconstruction of the phenomenon. The implications for future research related to the design of safer and cost-efficient structures are considerable.

CRediT authorship contribution statement

Federico Canepa: Formal analysisperformed the data analysis, prepared the manuscript and figures. **Massimiliano Burlando:** Supervision, Data curation co-supervised the study, co-reviewed the paper and was responsible for data collection. **Giovanni Solari:** Supervision supervised the study and reviewed the paper. All the three authors contributed to the preparation of the new (revised) version of the manuscript.

Declaration of competing interest

The authors declare that they have no known competing financial interests or personal relationships that could have appeared to influence the work reported in this paper.

Acknowledgments

This research is funded by the European Research Council (ERC) under the European Union's Horizon 2020 Research and Innovation Program (Grant agreement No. 741273) for the project THUNDERR – Detection, simulation, modelling and loading of thunderstorm outflows to design wind-safer and cost-efficient structures – supported by an Advanced Grant 2016. The data used for this research was recorded by the monitoring network set up as part of the European Projects Wind and Ports (grant No. B87E09000000007) and Wind, Ports and Sea (grant No. B82F13000100005), funded by the European Territorial Cooperation Objective, Cross-border program Italy-France Maritime 2007–2013.

References

Burlando, M., De Cio, A., Pizzo, M., Solari, G., 2017a. Analysis of wind vertical profiles of thunderstorm events in the mediterranean. In: 9th Asia-Pacific Conference on Wind Engineering, Auckland, New Zealand, p. 4.

Burlando, M., Romanić, D., Solari, G., Hangan, H., Zhang, S., 2017b. Field data analysis and weather scenario of a downburst event in Livorno, Italy, on 1 october 2012. Mon. Weather Rev. 145, 3507–3527. https://doi.org/10.1175/MWR-D-17-0018.1.

Burlando, M., Tizzi, M., Solari, G., 2017c. Characteristics of downslope winds in the liguria region. Wind Struct. 24, 613–635. https://doi.org/10.12989/WAS.2017.24.6.613.

Burlando, M., Zhang, S., Solari, G., 2018. Monitoring, cataloguing, and weather scenarios of thunderstorm outflows in the northern Mediterranean. Nat. Hazards Earth Syst. Sci. 18, 2309–2330. https://doi.org/10.5194/nhess-18-2309-2018.

Byers, H.R., Braham, R.R., 1948. Thunderstorm Structure and Circulation. J. Meteorol 5, 71–86. https://doi.org/10.1175/1520-0469(1948)005<0071:TSAC>2.0.CO;2.

Chen, L., Letchford, C.W., 2005. Proper orthogonal decomposition of two vertical profiles of full-scale nonstationary downburst wind speeds[lzcl]. J. Wind Eng. Ind. Aerod. 93, 187–216. https://doi.org/10.1016/j.jweia.2004.11.004.

Choi, E.C.C., 1999. Extreme wind characteristics over Singapore – an area in the equatorial belt. J. Wind Eng. Ind. Aerod. 83, 61–69. https://doi.org/10.1016/S0167-6105(99)00061-6.

Choi, E.C.C., 2004. Field measurement and experimental study of wind speed profile during thunderstorms. J. Wind Eng. Ind. Aerod. 92, 275–290. https://doi.org/10.1016/j.jweia.2003.12.001.

Choi, E.C., Hidayat, F.A., 2002. Dynamic response of structures to thunderstorm winds. Prog. Struct. Eng. Mater. 4, 408–416. https://doi.org/10.1002/pse.132.

Davenport, A.G., 1967. Gust loading factors. J. Struct. Div. 93, 11–34.

De Gaetano, P., Repetto, M.P., Repetto, T., Solari, G., 2014. Separation and classification of extreme wind events from anemometric records. J. Wind Eng. Ind. Aerod. 126, 132–143. https://doi.org/10.1016/j.jweia.2014.01.006.

Durañona, V., Sterling, M., Baker, C.J., 2007. An analysis of extreme non-synoptic winds. J. Wind Eng. Ind. Aerod. 95, 1007–1027. https://doi.org/10.1016/j.jweia.2007.01.014.

Elawady, A., Aboshosha, H., El Damatty, A., Bitsuamlak, G., Hangan, H., Elatar, A., 2017. Aero-elastic testing of multi-spanned transmission line subjected to downbursts. J. Wind Eng. Ind. Aerod. 169, 194–216. https://doi.org/10.1016/j.jweia.2017.07.010.

Fujita, T.T., 1981. Tornadoes and downbursts in the context of generalized planetary scales. J. Atmos. Sci. 38, 1511–1534.

Fujita, T.T., 1985. The Downburst - Microburst and Macroburst - Report of Projects NIMROD and JAWS.

Fujita, T.T., Wakimoto, R.M., 1983. Microburst in jaws depicted by Doppler radars, pam, and aerial photographs. In: 21st Conf. Radar Meteorol. Edmont. Alta Can, p. 8.

Gast, K.D., Schroeder, J.L., 2003. Supercell rear-flank downdraft as sampled in the 2002 thunderstorm outflow experiment. In: Proc. 11th Int. Conf. Wind Eng. Lubbock Tex.

Geerts, B., 2001. Estimating downburst-related maximum surface wind speeds by means of proximity soundings in new south wales, Australia. Weather Forecast. 16, 9.

Goff, R.C., 1976. Vertical structure of thunderstorm outflows. Mon. Weather Rev. 104.

Gomes, L., Vickery, B.J., 1978. Extreme wind speeds in mixed wind climates. J. Wind Eng. Ind. Aerod. 2, 331–344. https://doi.org/10.1016/0167-6105(78)90018-1.

Gunter, W.S., Schroeder, J.L., 2015. High-resolution full-scale measurements of thunderstorm outflow winds. J. Wind Eng. Ind. Aerod. 138, 13–26. https://doi.org/10.1016/j.jweia.2014.12.005.

Hjelmfelt, M.R., 1988. Structure and life cycle of microburst outflows observed in Colorado. J. Appl. Meteorol. 27, 900–927.

Holmes, J.D., Hangan, H.M., Schroeder, J.L., Letchford, C.W., Orwig, K.D., 2008. A forensic study of the Lubbock-Reese downdraft of 2002. Wind Struct. 11, 137–152. https://doi.org/10.12989/WAS.2008.11.2.137.

Kasperski, M., 2002. A new wind zone map of Germany. J. Wind Eng. Ind. Aerod. 90, 1271–1287. https://doi.org/10.1016/S0167-6105(02)00257-X.

Letchford, C.W., Mans, C., Chay, M.T., 2002. Thunderstorms—their importance in wind engineering (a case for the next generation wind tunnel). J. Wind Eng. Ind. Aerod. 90, 1415–1433. https://doi.org/10.1016/S0167-6105(02)00262-3.

Lombardo, F.T., Smith, D.A., Schroeder, J.L., Mehta, K.C., 2014. Thunderstorm characteristics of importance to wind engineering. J. Wind Eng. Ind. Aerod. 125, 121–132. https://doi.org/10.1016/j.jweia.2013.12.004.

Mann, J., Peña, A., Bingöl, F., Wagner, R., Courtney, M.S., 2010. Lidar scanning of momentum flux in and above the atmospheric surface layer. J. Atmos. Ocean. Technol. 27, 959–976. https://doi.org/10.1175/2010JTECHA1389.1.

Orwig, K.D., Schroeder, J.L., 2007. Near-surface wind characteristics of extreme thunderstorm outflows. J. Wind Eng. Ind. Aerod. 95, 565–584. https://doi.org/10.1016/j.jweia.2006.12.002.

Ponte Jr., J., Riera, J.D., 2007. Wind velocity field during thunderstorms. Wind Struct. 10, 287–300. https://doi.org/10.12989/WAS.2007.10.3.287.

Repetto, M.P., Burlando, M., Solari, G., De Gaetano, P., Pizzo, M., Tizzi, M., 2018. A web-based GIS platform for the safe management and risk assessment of complex structural and infrastructural systems exposed to wind. Adv. Eng. Software 117, 29–45. https://doi.org/10.1016/j.advengsoft.2017.03.002.

Romanic, D., Parvu, D., Hangan, H., 2017. Influence of background winds and storm motion on downburst outflow. In: Presented at the 7th European and African Conference on Wind Engineering (EACWE 2017), Liège, Belgium, p. 2.

Romanic, D., Hangan, H., 2019. The interplay between background atmospheric boundary layer winds and downburst outflows. A first physical experiment. In: Ricciardelli, F., Avossa, A.M. (Eds.), Proceedings of the XV Conference of the Italian

Association for Wind Engineering. Springer International Publishing, Cham, pp. 652–664. https://doi.org/10.1007/978-3-030-12815-9_49.
Sathe, A., Mann, J., Gottschall, J., Courtney, M.S., 2011. Can wind lidars measure turbulence? J. Atmos. Ocean. Technol. 28, 853–868. https://doi.org/10.1175/JTECH-D-10-05004.1.
Sathe, A., Mann, J., 2013. A review of turbulence measurements using ground-based wind lidars. Atmospheric Meas. Tech. 6, 3147–3167. https://doi.org/10.5194/amt-6-3147-2013.
Smith, D.A., Harris, M., Coffey, A.S., Mikkelsen, T., Jørgensen, H.E., Mann, J., Danielian, R., 2006. Wind lidar evaluation at the Danish wind test site in Høvsøre. Wind Energy 9, 87–93. https://doi.org/10.1002/we.193.
Solari, G., 2019. Wind Science and Engineering: Origins, Developments, Fundamentals and Advancements. Springer International Publishing.
Solari, G., Piccardo, G., 2001. Probabilistic 3-D turbulence modeling for gust buffeting of structures. Probabilist. Eng. Mech. 16, 73–86. https://doi.org/10.1016/S0266-8920(00)00010-2.
Solari, G., Repetto, M.P., Burlando, M., De Gaetano, P., Pizzo, M., Tizzi, M., Parodi, M., 2012. The wind forecast for safety management of port areas. J. Wind Eng. Ind. Aerod. 104–106, 266–277. https://doi.org/10.1016/j.jweia.2012.03.029.
Solari, G., Burlando, M., De Gaetano, P., Repetto, M.P., 2015a. Characteristics of thunderstorms relevant to the wind loading of structures. Wind Struct. 20, 763–791. https://doi.org/10.12989/WAS.2015.20.6.763.
Solari, G., De Gaetano, P., Repetto, M.P., 2015b. Thunderstorm response spectrum: fundamentals and case study. J. Wind Eng. Ind. Aerod. 143, 62–77. https://doi.org/10.1016/j.jweia.2015.04.009.
Solari, G., Burlando, M., Repetto, M.P., 2020. Detection, simulation, modelling and loading of thunderstorm outflows to design wind-safer and cost-efficient structures. J. Wind Eng. Ind. Aerod. 200, 104142 https://doi.org/10.1016/j.jweia.2020.104142.
Thom, H.C.S., 1968. New distributions of extreme winds in the United States. J. Struct. Div. 94, 1787–1802.
Tubino, F., Solari, G., 2020. Time varying mean extraction for stationary and nonstationary winds. J. Wind Eng. Ind. Aerod. 203, 104187. https://doi.org/10.1016/j.jweia.2020.104187.
Wakimoto, R.M., 1982. The life cycle of thunderstorm gust fronts as viewed with Doppler radar and rawinsonde data. Mon. Weather Rev. 110, 1060–1082.
Wilczak, J.M., Gossard, E.E., Neff, W.D., Eberhard, W.L., 1996. Ground-based remote sensing of the atmospheric boundary layer: 25 years of progress. Bound.-Layer Meteorol. 78, 321–349. https://doi.org/10.1007/BF00120940.
Zhang, S., Solari, G., Yang, Q., Repetto, M.P., 2018a. Extreme wind speed distribution in a mixed wind climate. J. Wind Eng. Ind. Aerod. 176, 239–253. https://doi.org/10.1016/j.jweia.2018.03.019.
Zhang, S., Solari, G., De Gaetano, P., Burlando, M., Repetto, M.P., 2018b. A refined analysis of thunderstorm outflow characteristics relevant to the wind loading of structures. Probabilist. Eng. Mech. 54, 9–24. https://doi.org/10.1016/j.probengmech.2017.06.003.
Zhang, S., Solari, G., Burlando, M., Yang, Q., 2019. Directional decomposition and properties of thunderstorm outflows. J. Wind Eng. Ind. Aerod. 189, 71–90. https://doi.org/10.1016/j.jweia.2019.03.014.